



UPPSALA
UNIVERSITET

*Digital Comprehensive Summaries of Uppsala Dissertations
from the Faculty of Science and Technology 2120*

Detection of Bio-analytes with Streaming Current

From Fundamental Principles to Novel Applications

SIDDHARTH S. SAHU



ACTA
UNIVERSITATIS
UPSALIENSIS
UPPSALA
2022

ISSN 1651-6214
ISBN 978-91-513-1419-8
URN urn:nbn:se:uu:diva-467813

Dissertation presented at Uppsala University to be publicly examined in Siegbahnsalen, Ångströmlaboratoriet, Lägerhyddsvägen 1, Uppsala, Friday, 8 April 2022 at 09:00 for the degree of Doctor of Philosophy. The examination will be conducted in English. Faculty examiner: Professor Michel Calame (University of Basel, Switzerland).

Abstract

Sahu, S. S. 2022. Detection of Bio-analytes with Streaming Current. From Fundamental Principles to Novel Applications. *Digital Comprehensive Summaries of Uppsala Dissertations from the Faculty of Science and Technology* 2120. 89 pp. Uppsala: Acta Universitatis Upsaliensis. ISBN 978-91-513-1419-8.

A biosensor based on streaming current is a new and relatively unexplored subject with significant potential. This thesis attempts to gain a deeper understanding of the governing principles, and then exploit them to further improve its performance as well as develop novel applications. To this end, the underlying theoretical frameworks were examined and two critical parameters of the target: its size and electric charge, influencing the sensor's sensitivity were identified. This was followed by experimental evaluation of the parameters, using a set of tailor-made proteins, aiming to understand the nature and extent of their influence on the sensor response in relation to simulation performed following an established model.

The dependence of the sensor response on the charge of an analyte, or specifically the charge contrast between the sensor surface and an analyte, opens a new avenue to improve the sensitivity and also to develop novel functionality. First, this aspect was exploited to improve the sensitivity by optimizing the surface functionalization strategy. Three such methods were compared in terms of the resulting zeta potential of the surface. The sensitivity was the highest when the charge contrast was maximum. The optimal functionalization strategy was then used for highly sensitive detection of extracellular vesicles (EVs), where an improvement in the limit of detection by two orders of magnitude over the previously reported results was demonstrated. Two applications of the improved method were then demonstrated: monitoring the effectiveness of targeted cancer medicines and analysis of liquid biopsy of cancer patients via sensitive profiling of EV-membrane proteins.

Improvement in the detection specificity is a critical aspect of biosensing. This was achieved by implementing a sandwich immunoassay and demonstrating the proof of concept using trastuzumab as the target and Z-domain as both the capture and detection probes. Although the improved selectivity came at the cost of a lower sensitivity, this could be mitigated via DNA-conjugation with the detection probes, a novel electrostatic labelling strategy that allows for improvement of the sensitivity by exploiting the electrostatic influence. An application of this method was then demonstrated by detecting the target from a complex medium of *E. coli* cell lysate. Continuing the prospect of charge engineering of antibodies, a set of positively and negatively charged antibodies were synthesized by conjugating poly-lysine and DNA oligonucleotides, respectively. This enabled stepwise, multiplexed membrane protein analysis of EVs using the alternating charge-labelled antibodies. The method was then applied to investigate EV-heterogeneity.

Keywords: Streaming current, Electrokinetic biosensor, Size and Charge effects, membrane protein profiling of extracellular vesicles, sandwich immunoassay, charge-labelled antibodies, multiplexed detection, exosome heterogeneity

Siddharth S. Sahu, Department of Electrical Engineering, Solid-State Electronics, Box 534, Uppsala University, SE-751 21 Uppsala, Sweden.

© Siddharth S. Sahu 2022

ISSN 1651-6214

ISBN 978-91-513-1419-8

URN urn:nbn:se:uu:diva-467813 (<http://urn.kb.se/resolve?urn=urn:nbn:se:uu:diva-467813>)

To all who have made a contribution to science.

List of publications

This thesis is based on the following papers, which are referred to in the text by their Roman numerals.

- I. **Sahu, S. S.**, Stiller, C., Cavallaro, S., Karlström, A. E., Linnros, J., and Dev, A. (2020). Influence of molecular size and zeta potential in electrokinetic biosensing. *Biosensors and Bioelectronics*, 152, 112005.
- II. **Sahu, S. S.**, Cavallaro, S., Hååg, P., Nagy, A., Karlström, A. E., Lewensohn, R., Viktorsson, K., Linnros, J., and Dev, A. (2021). Exploiting Electrostatic Interaction for Highly Sensitive Detection of Tumor-Derived Extracellular Vesicles by an Electrokinetic Sensor. *ACS Applied Materials & Interfaces*, 13(36), 42513-42521.
- III. **Sahu, S. S.**, Stiller, C., Gomero, E. P., Nagy, Á., Karlström, A. E., Linnros, J., and Dev, A. (2021). Electrokinetic sandwich assay and DNA mediated charge amplification for enhanced sensitivity and specificity. *Biosensors and Bioelectronics*, 176, 112917.
- IV. **Sahu S. S.**, Gevari, M. T., Nagy, Á., Gestin, M., Karlström, A. E., Hååg, P., Viktorsson, K., Linnros, J., and Dev, A. (2022). Multi-marker profiling of extracellular vesicles with an electrokinetic sensor via electrostatic labeling. *Manuscript*.
- V. Gevari, M. T., **Sahu, S. S.**, Mitra, D., Linnros, J., and Dev, A. (2022). Microchip-based electrokinetic biosensor: microfabrication and application in membrane protein profiling of extracellular vesicles. *Manuscript*.

Reprints were made with permission from the respective publishers.

Author's contributions

- I. Study conceptualization, sensor surface functionalization, electrokinetic measurements, ELS measurements, data analysis, simulations, writing the original manuscript, revision and editing
- II. Study conceptualization, development and optimization the functionalization steps, electrokinetic measurements, data analysis, simulations, writing the original manuscript, revision and editing
- III. Study conceptualization, sensor surface functionalization, electrokinetic measurements, ELS measurements, data analysis, simulations, writing the original manuscript, revision and editing
- IV. Study conceptualization, chip level functionalization, chip level electrokinetic measurements, data analysis, simulations, writing the original manuscript
- V. Part of the chip functionalizations, part of the measurements, part of the data analysis, editing the manuscript

Publications not included in the thesis

- I. Cavallaro, S., Horak, J., Hååg, P., Gupta, D., Stiller, C., **Sahu, S. S.**, Görgens, A., Gatty, H. K., Viktorsson, K., El Andaloussi, S., Lewensohn, R., Karlström, A. E., Linnros, J., and Dev, A. (2019). Label-free surface protein profiling of extracellular vesicles by an electrokinetic sensor. *ACS sensors*, 4(5), 1399-1408.
- II. Cavallaro, S., Pevero, F., Stridfeldt, F., Görgens, A., Paba, C., **Sahu, S. S.**, Mamand, D. R., Gupta, D., Linnros, J., and Dev, A. (2021). Multiparametric profiling of single nanoscale extracellular vesicles by combined atomic force and fluorescence microscopy: correlation and heterogeneity in their molecular and biophysical features. *Small*, 17(14), 2008155.
- III. Cavallaro, S., Hååg, P., **Sahu, S. S.**, Berisha, L., Kaminsky, V. O., Ekman, S., Lewensohn, R., Linnros, J., Viktorsson, K., and Dev, A. (2021). Multiplexed electrokinetic sensor for detection and therapy monitoring of extracellular vesicles from liquid biopsies of non-small-cell lung cancer patients. *Biosensors and Bioelectronics*, 193, 113568.

Contents

1. Introduction.....	13
1.1 A brief history of biosensors	13
1.2 Emergence of point-of-care biosensing.....	14
1.3 Scope of the thesis.....	15
2. Theoretical background	17
2.1 The intricate interplay of currents	17
2.2 The electrical double layer	21
2.3 Flow under a steady external pressure	22
2.4 Modelling the streaming current for non-ideal surfaces.....	23
2.5 Hydrodynamic radii of proteins	25
2.6 Electrophoretic light scattering (ELS).....	26
2.7 Extracellular vesicles: what makes them particularly suitable targets for our sensor?	27
2.8 How do we express the signal?	27
2.9 Differential measurement with trapezoidal pulses	28
3. Influence of the size and charge of a target	30
3.1 How does the binding of the target molecules modify the surface properties?	30
3.2 The model system.....	31
3.3 Theoretical predictions.....	32
3.4 Experimental validation of the simulations	34
3.4.1 Surface functionalization	34
3.4.2 Fluidic and electrical measurements.....	35
3.4.3 How well do the results agree with simulations?	36
3.5 A closer look at the apparent discrepancy	38
3.6 Modulating the signal via pH	39
3.7 Does the sensor have a unique limit of detection?	41
3.8 Chapter Summary.....	43
4. Improving Sensitivity by Surface Charge Optimization	44
4.1 Signal enhancement in surface based sensors	44
4.2 Experimental setup	44
4.3 Surface functionalization strategies.....	45
4.3.1 Protocol details	45
4.3.2 Non-specific binding (NSB) and negative control	46

4.3.3 Initial zeta potential of the surface and signal enhancement	47
4.3.4 Surface roughness.....	48
4.4.5 Simulations support the results	49
4.5 Limit of detection	50
4.6 Examining a possible concern.....	50
4.7 Applications	51
4.7.1 Treatment monitoring	52
4.7.1 Liquid biopsy with reduced sample volume	54
4.8 Surface charge density	55
4.9 Chapter summary	56
5. Electrokinetic Sandwich Assay.....	57
5.1 Improving sensing selectivity.....	57
5.2 Direct assay vs. sandwich assay and the model system	57
5.3 Proof of principle of an electrokinetic sandwich assay	58
5.4 Signal enhancement by DNA conjugation	61
5.5 Simulations.....	62
5.6 DNA-conjugation and affinity.....	64
5.7 Application: detection of target from a complex medium.....	65
5.8 Chapter Summary.....	67
6. Multiplexed membrane protein profiling of extracellular vesicles using charge-labelled antibodies	68
6.1 Micro-chip based sensing.....	69
6.2 A labelling strategy for multi-marker membrane profiling.....	70
6.3 Electrostatic labels and proof of concept study.....	70
6.4 sEVs membrane protein profiling: biased vs. unbiased capture.....	72
6.5 Multi-marker profiling of extracellular vesicles.....	74
6.6 Chapter summary	75
7. Summary and Outlook	77
Samfattning på svenska.....	80
Acknowledgements.....	82
References.....	84

Symbols

I_C	conduction current
I_F	Faradic current
I_{ext}	external current
I_S	streaming current
I_{S0}	streaming current of the (initial) bare channel
ζ	zeta potential
ζ^*	apparent surface zeta potential
ζ_i^*	apparent surface zeta potential of the (initial) bare channel
ζ_p	molecular zeta potential
a	radius of the particle
a_r	normalized radius of the particle
λ	Debye length / EDL thickness
η	dynamic viscosity
ϵ	relative permittivity
ϵ_0	permittivity of free space
E	electric field
S_i	sensitivity
μ_E	electrophoretic mobility
θ	surface coverage
L	length of the channel
A	area of cross section of the channel
P	external pressure
R	radius of the channel
Q	volumetric flow rate
u	fluid velocity
ρ	fluid density
σ	electrostatic charge density
σ_{eff}	effective charge density
R_C	universal gas constant
F	Faraday's constant
i_c	ionic strength
ϕ	electrostatic potential
C_i	macroscopic flow perturbation parameter
C_p	electrical charge density perturbation parameter

Abbreviations

AFM	atomic force microscope
APTES	(3-aminopropyl)triethoxy silane
EDL	electrical double layer
EGFR	epidermal growth factor receptor
(s)EV	(small) extracellular vesicle
GA	glutaraldehyde
ISFET	ion selective field effect transistor
LOD	limit of detection
MDS	minimum detectable signal
NSCLC	non-small cell lung cancer
PBS	phosphate buffered saline
PD-L1	programmed death-ligand 1
PE	pleural effusion
PEG	polyethyl glycol
PLL	poly-L-lysine
PPB	PLL grafted biotinylated PEG
POC	point of care
NSB	non-specific binding
SD	standard deviation
SEC	size exclusion chromatography
SPPS	solid state peptide synthesis
SPR	surface plasmon resonance
SR	specificity ratio

1. Introduction

1.1 A brief history of biosensors

Biosensors owe their origin to the early 1900s when a lot of groundwork was laid down, forming the basis for the rapid growth of the field in the latter half of the century [1]. The concept of pH was introduced by Søren Sørensen in 1909 and this was followed, in 1921, by the realization of the first ever electrode for pH measurements by W. S. Hughes [2]. Enzyme immobilization on an aluminium hydroxide surface was demonstrated by Griffin and Nelson around the same time [3], [4]. The first ever true biosensor was then developed by Leland Clark[5] in 1953 to measure the blood oxygen levels using a platinum electrode. The oxygen molecules reach the Pt. cathode through a permeable membrane such as cellophane, and undergo a chemical reaction where each oxygen molecule generates four electrons, leading to a current. Clark et. al. wrote [5], *“After many unsuccessful attempts to obtain a stable, reproducible electrode for use in whole blood, an electrode consisting of a platinum surface covered with a cellophane membrane was devised and studied under various conditions...”*. Here, Clark highlights two key features for a biosensing method aspiring to real world use, namely stability and reproducibility. This fact remains relevant even today. Biosensors have seen tremendous growth in the last seven decades. Around the late 1900s, silicon was realized to be a very suitably material for the next generation of biosensors, making it possible to design biosensors that were low cost, smaller sized, rapid, reliable and the possibility to be integrated on-chip [6]. The ion-selective field effect transistor (ISFET) was invented in 1970 [7] and marked an important milestone. It was the precursor to BioFETs developed later, that marked the integration of biologically active materials with an ISFET [6]. This was followed, in 1975, by the first ever commercial biosensor for glucose detection by Yellow Spring Instruments [8]. In 1983, the development of the surface plasmon resonance (SPR) immunosensor [9] marked yet another key milestone. It paved the way for the development for the first SPR-based biosensor by Biacore [10] in 1990. In 2006, single-molecule level of detection was achieved through spectro-electrochemistry [11].

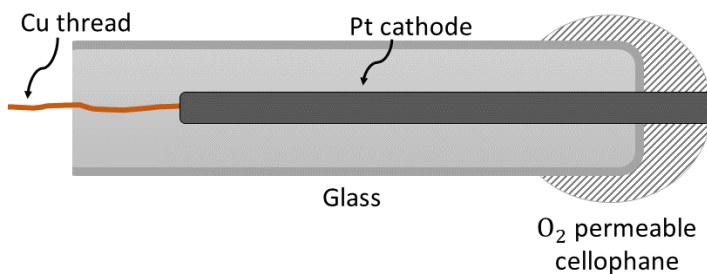


Figure 1.1: The first ever biosensor developed by Clark et. al., now known as the Clark electrode, measured the blood oxygen tension. It consisted of a platinum cathode in glass along with an O_2 permeable cellophane.

Nowadays, there is a large variety of biosensors based on various methods and serving different niche areas. This has been motivated by the demand for such devices as the repertoire of biomarkers that need to be detected is ever-increasing. Biosensors have found application in healthcare [12]–[14], environmental safety [15], [16], food safety [17], [18], and so on. This rapid progress has also brought on new challenges. Diffusion and kinetic limited interactions, on the other hand, provide limitations to the response time for low concentrations of the analyte [19]. Overcoming this, by using electric fields for instance, is usually not possible without considerably increasing the sensor complexity [20]. Moreover, several of the so-called ultra-sensitive sensors have failed in real world applications due to high cross-reactivity [21]. This also presents a major hurdle in scaling up of multiplexed sensors [21].

1.2 Emergence of point-of-care biosensing

A major area of research in the last decade has been the development of sensors that can function at the point-of-care (POC) for early diagnosis and efficient therapy monitoring. This has led to an increased focus on biosensors that are portable, cost-effective, simple, fast, sensitive and selective so that they are usable by anyone without specialized knowledge [22]. Several different biosensing methods have been studied for potential POC applications. These include optical [23], electrochemical [24], paper and flexible substrates based [25] sensors. Advancements in wireless technology has ushered in the era of implantable, wearable and hand-held biosensing devices [26]. This has opened up the possibility of continuous monitoring of medically important metrics, metabolites and other bio-markers. This would lead to more efficient management of diseases like various cancers, diabetes and Alzheimer's [26]. The pandemic caused by the SARS-CoV-2 virus has further accelerated the development of POC biosensors [27]. It is estimated that the demand for POC biosensors shall continue to rise in the coming decades. Hence, further research and

development in this area is paramount. The global biosensors industry was valued at 22.4 billion USD and is expected to grow at 7.9% annually until 2028 [28]. A major demand driver of this growth are POC biosensors. To this end, electrokinetic biosensing such as streaming current/potential are promising methods for developing POC devices of the future. As we shall discuss in the latter parts of the thesis, the streaming current method makes it possible to develop highly sensitive sensors while meeting the criteria listed earlier.

1.3 Scope of the thesis

This thesis first focuses on the influence of size and charge of the targets on the signal in an electrokinetic biosensor relying on the streaming current method. This was carried out using experiments and the results were validated using an existing theoretical model in the literature. Strategies were also identified for enhancing the sensitivity by modulating the charge in various ways: changing the pH of the measuring buffer, via DNA-conjugation, and using alternative surface functionalization methods. The scope of this biosensing method was further expanded by demonstrating the proof of principle of an electrokinetic sandwich assay. Due to their diagnostic importance as a source of biomarkers for various kinds of cancer, extracellular vesicles were used to demonstrate applications of several of the techniques covered in this thesis. They were used to demonstrate the improved sensitivity with alternative functionalization strategies, as well as to show multi-marker profiling of proteins on their surface, allowing the analysis of sEV heterogeneity across different sub-populations. This opens up the possibility of clinical applications of this biosensing method.

Chapter 2 introduces the underlying theoretical background and working principle of the various methods used.

Chapter 3 deals with the influence of the size and charge of the target, signal enhancement by modulating the pH, validation of the results through simulations, and shows how the limit of detection depends on the target.

Chapter 4 explores the possibility to enhance the signal by modulating the surface charge of the sensor. This was achieved by using various functionalization strategies. The resulting signal improvement was backed by simulations and is used to demonstrate highly sensitive monitoring of cancer treatments as well as the clinically important liquid biopsy with significantly small sample volumes.

Chapter 5 explains the concept of an electrokinetic sandwich assay, its comparison with the direct assay, signal enhancement via DNA-conjugation with the detection probes, and demonstrates an application by detecting the target from a complex medium.

Chapter 6 discusses a method to analyse sEV heterogeneity, by demonstrating the profiling of multiple surface proteins of extracellular vesicles using electrostatic labels.

Finally, chapter 7 concludes the thesis and provides an outlook for future work based on the results.

2. Theoretical background

2.1 The intricate interplay of currents

The streaming current method of biosensing can appear particularly challenging to understand at the first glance, as it is also accompanied by several other kinds of currents co-existing in the same channel. Let's start by understanding the streaming current (I_S), that lies at the core of it all. It is generated whenever an electrolyte is made to flow under a pressure gradient, through a channel made of charged walls. Although the bulk of the electrolyte is electro-neutral in the absence of an external electric field, there still exists a charge imbalance at the solid-liquid interface as illustrated in figure 2.1. This is due to the immobile charges accumulated on the channel walls due to ionization of the surface groups. Under a pressure gradient, the flow of the electrolyte across the pressure gradient leads to a net flow of ions accumulated along the interface, setting up the streaming current. The channel then effectively works as a battery, and can drive an external current when connected to circuit. The red arrows indicate a parabolic flow profile, that obeys the Hagen-Poiseuille conditions, discussed in detail in section 2.3.

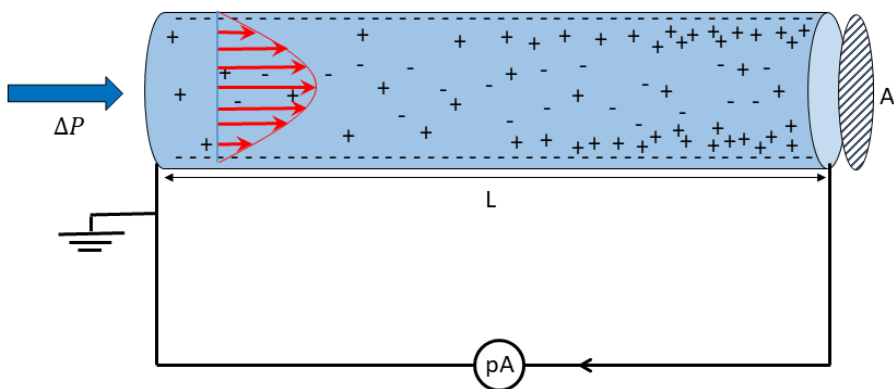


Figure 2.1. A schematic representation of the generation of the streaming current in a cylindrical channel with charged walls when an electrolyte is allowed to flow through it under an external pressure. The red arrows indicate the Poiseuille flow of the fluid.

The streaming current leads to an accumulation of the counter-ions at the outlet, leading to the build-up of a potential, known as the streaming potential. In the absence of an external circuit, the streaming potential drives the flow of the counter ions in the opposite direction to that of the streaming current, and through the bulk of the electrolyte. This leads to the conduction current, I_C . When steady state is achieved, I_C would hence be equal to I_S . If we wish to measure I_S , we would need to connect the channel to an external source-meter through an electrode. This would lead to a splitting of I_S as the streaming potential would also drive a current through the external circuit, which we shall hereafter refer to as the Faradic current, I_F . The origin of I_S , I_C , and I_F in a channel along with its equivalent electrical circuit are shown in figure 2.2. Kirchoff's current law [29] dictates that:

$$I_S = I_C + I_F \quad \dots(2.1)$$

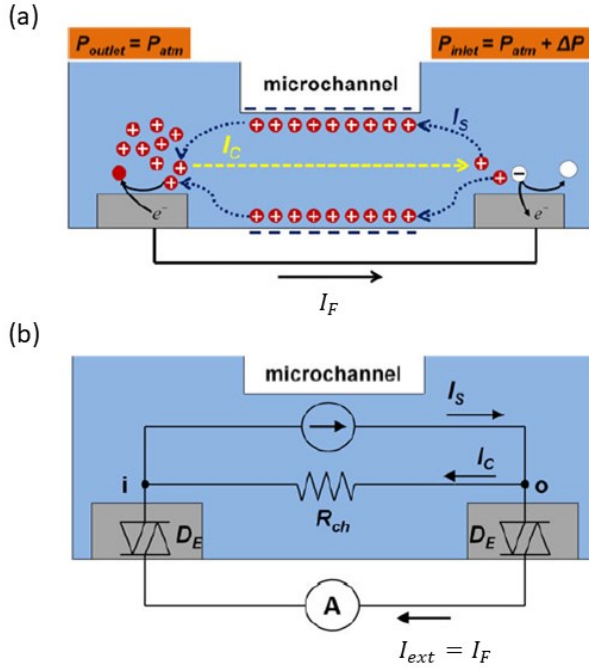


Figure 2.2 (a) The origin of the streaming current (I_S), conduction current (I_C) and the Faradic current (I_F) across a microchannel connected to an external circuit via electrodes at the inlet and outlet. (b) An equivalent electrical circuit of this schematic, representing the channel as a resistor with resistance R_{ch} , and the electrodes as parallel diodes with opposite polarities (D_E). In case of polarizable electrodes, there is also a capacitor, C_E in parallel to the diodes. Images adapted with permission from ref. [30], © 2013, Springer-Verlag Berlin Heidelberg.

In order to accurately measure I_S , we would ideally want I_C to be 0, so that $I_F = I_S$. In practice, this depends on the polarizability of the electrodes [30], which in turn depends on the efficiency of the redox process on the electrode surface in comparison to the impedance, R_{ch} offered by the electrolyte to I_C . In essence, electrode can be modelled as two parallel, oppositely polarized electrodes connected in parallel to a capacitor. The diode models the charge transfer across the interface of the electrode while the capacitor models the charge accumulation on its surface. There is hence a charging and discharging associated to the flow of the current through the electrode. Assuming the current recorded by the source-meter, $I_{ext} = I_F$, if the electrodes possess a lower degree of polarizability, I_C is small and $I_S \sim I_F$. For a highly polarizable electrode on the other hand, I_{ext} is small and $I_S \sim I_C$. This is schematically illustrated in figure 2.3 in terms of the transfer curves. Another way of looking at this is in terms of the impedances. For a non-polarizable electrode, the redox process on the electrode surface is not enough to compete with the transport of I_C through the electrolyte, we have $R_{ch} \gg 2R_E$, with R_E being the electrode impedance. Then, an accurate measurement of I_S is possible. On the other hand, if the efficiency of the redox process is less than or comparable to that of the conduction of ions through the bulk, we have a polarizable electrode, and either $R_{ch} \ll 2R_E$ or the two quantities are comparable respectively. Then, a measurement of the streaming current is affected by the charging and discharging of the electrodes.

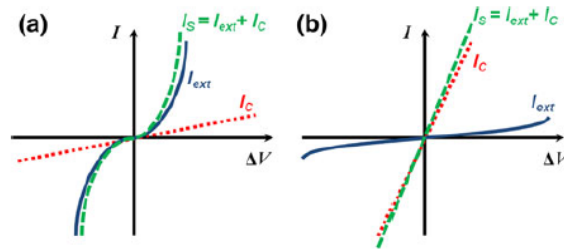


Figure 2.3. Schematic representation of the transfer curves, depicting the current components resulting from the equivalent circuit shown in figure 2.2. (a) Measurements made with non-polarizable electrodes leads to very low conduction current, as a result of which the measured quantity, I_{ext} is closer to the value of I_S . (b) This is not the situation when highly polarizable electrodes are used, as a result of which, I_{ext} is much smaller than I_S , leading to large underestimation of I_S . Images reproduced with permission from ref. [30], © 2013, Springer-Verlag Berlin Heidelberg.

Both the scenarios depicted in the figure 2.3 were observed in our measurements with platinum electrodes. When the electrodes were thoroughly cleaned, their polarizability was minimal. However, when there is accumulation of impurities on their surface, they became highly polarizable as the im-

purities usually are insulating in nature. Figure 2.4 compares I_{ext} under a trapezoidal pressure waveform (see figure 2.8) when the electrodes clean and contaminated respectively. Applying a trapezoidal flow profile then leads to transient curves in the measured I_{ext} , as shown in figure 2.4. The figure shows measured values of I_{ext} when the electrode exhibited very low levels of polarizability vs. when it was rather highly polarizable. In the first case, the value of I_{ext} is very close to the value of I_S due to minimal charging and discharging effects of the electrodes. On the other hand, when the electrodes showed strong charging and discharging effects, the value of I_{ext} was the closest to I_S only at the beginning of each pulse, after which it dropped as the electrodes accumulated charge. In principle, the height of the initial part of each pulse should be the same if the surface is in steady state. However, the measured pulses were of variable heights due to the fact that the sampling rate of the sourcemeter was quite small due to the extremely small values of the current measured (in the range of ~ 100 pA). Hence, the data point corresponding to the very beginning of each pulse was not perfectly captured. This observation provided a reliable method to test the cleanliness of the electrodes at the beginning of each measurement. If the profile of I_{ext} appeared similar to figure 2.4b, a thorough cleaning of the electrodes was done. For the rest of the thesis, it is assumed that $I_{ext} = I_S$.

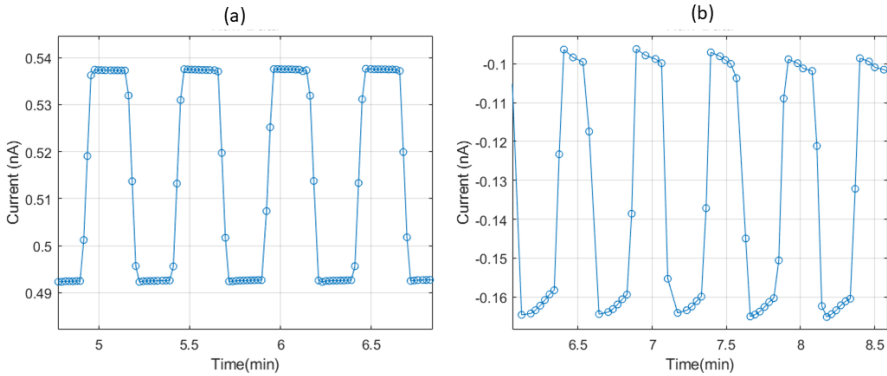
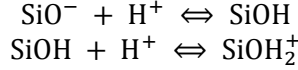


Figure 2.4 Measurements of the I_{ext} corresponding to a trapezoidal pressure pulse applied across the capillary, when the electrodes demonstrated (a) low polarizability, indicated by the flat plateaus of the I_{ext} (b) high polarizability, indicated by the presence of peaks. Ideally, I_{ext} should follow the profile of the external pressure, but due to charging and discharging of the electrodes in (b), this was not the case.

An additional conduction route exists when the connection to the external circuit is established: the silica surface itself [31]. This surface conduction current can also affect the measurement of I_{ext} . However, it is negligible if the channel conductance is large enough. This is true in our case as the channel dimensions and the electrolyte conductivity are large enough.

2.2 The electrical double layer

The streaming current owes its existence to the presence of the electrical double layer (EDL) at the solid-liquid interface of the sensor. When the silica surface is exposed to an aqueous electrolyte, the EDL is formed due to the following protonation and deprotonation reactions [32]:



These reactions eventually reach equilibrium, and result in the accumulation of the surface charge. This is compensated by a diffuse layer of counter-ions formed in the liquid, whereas the co-ions are repelled away from the surface. The distribution of the ions is governed by the Poisson-Boltzmann statistics. The latter is obtained by substituting the expression for the charge density from the Boltzmann statistics into the Poisson equation, resulting in the following relation [33]:

$$\nabla^2 \phi = -\frac{\sigma}{\epsilon} - \frac{F}{\epsilon} \sum_i c_{i,\infty} z_i \exp\left(-\frac{z_i F \phi}{R_c T}\right) \quad \dots(2.2)$$

where, ϕ is the electrostatic potential, σ is the electrostatic charge density, F is Faraday's constant, ϵ is the permittivity, $c_{i,\infty}$ is the concentration of the ions in the bulk, z_i is the valency of the ions, R_c is the universal gas constant and T is the temperature. Equation 2.2 can be solved either to obtain the full solution, or in certain limits in order to obtain an approximate solution. The most common approximation, known as the Debye-Hückel approximation, can be used for small values of the interface potential, allowing us to solve a linearized version of equation 2.2. In any case, the solutions to the Poisson-Boltzmann equation describe an exponentially decreasing nature of the electrical potential as we move from the interface to the bulk portion of the electrolyte. It implies that the charge of the interface is "screened" or hidden by the ions in the solution. The same happens if any charged molecule is introduced into the channel - the co-ions and counter-ions rearrange themselves in order to screen its charge. The strength of this screening is quantified by the term Debye length (λ). Also known as the thickness of the electrical double layer, it is defined by the expression:

$$\lambda = \sqrt{\frac{\epsilon R_c T}{2 F^2 i_c}} \quad \dots(2.3)$$

where i_c is the ionic strength in the bulk. A simplified picture of the charge screening and the formation of the EDL is shown in figure 2.5.

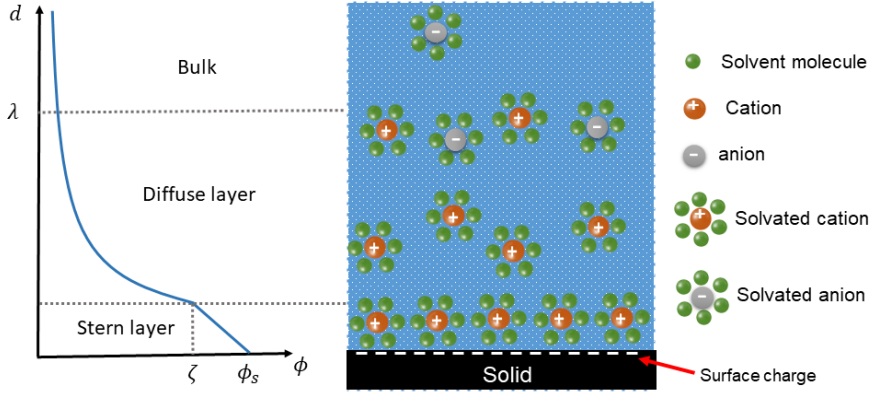


Figure 2.5. A schematic representation of the electrical double layer forming at the solid-liquid interface. In addition to the ions arranging themselves according to the Poisson-Boltzmann statistics, each ion is also surrounded by the solvent molecules, as process known as solvation. A schematic representation of the electrostatic potential, ϕ as a function of the distance, d from the surface is also shown.

2.3 Flow under a steady external pressure

The flow of a viscous fluid in general is described by a partial differential equation called the Navier-Stokes equation [33]. The flow can be classified based on the geometry of the channel and other conditions. If the flow is laminar and between two moving plates, it is called Couette flow, while a laminar flow through a channel under a steady, non-zero external pressure is called a Poiseuille flow [33]. Furthermore, if the cross-section in the latter case is circular, it is specifically known as Hagen-Poiseuille flow, which is applicable to our case. We can now proceed to solve this equation in order to obtain the expression governing the flow of the fluid. We start with the complete Navier-Stokes equation [33], given by:

$$\rho \frac{\partial \mathbf{u}}{\partial t} + \rho \mathbf{u} \cdot \nabla \mathbf{u} = -\nabla P + \eta \nabla^2 \mathbf{u} \quad \dots(2.4)$$

where ρ is the fluid density, P is the steady external pressure, \mathbf{u} is the fluid velocity and η is its dynamic viscosity. In order to solve this equation, we make the following assumptions: the flow is laminar, in a steady state, and in an infinitely long channel. Steady state flow implies that there is no acceleration of the fluid particles. Hence, the first term in equation 2.4 is zero. Laminar

flow implies that there is no mixing, and the flow is one dimensional. Therefore, the second term in equation 2.4, also known as the convective term, becomes zero. Equation 2.4 now gets simplified to:

$$\nabla P = \eta \nabla^2 \mathbf{u} \quad \dots(2.5)$$

As we are solving for a circular cross section, it is easier to do so in the cylindrical coordinate system, to take advantage of the radial symmetry. We can then express the one-dimensional fluid velocity, u_z as:

$$u_z(r) = -\frac{1}{4\eta} \frac{\partial P}{\partial z} (R^2 - r^2) \quad \dots(2.6)$$

where r is the coordinate along the radial direction, and z is the coordinate along the axis of the flow and R is the radius of the channel. It is important to note that for an analyte covered surface of the channel, equation 2.6 holds only if the radius of the analyte is negligible in comparison to R , which is true in our case. The equation indicates that u_z has a quadratic dependence on r . The fluid molecules thus follow a parabolic flow profile in the cylindrical channel, as indicated in figure 2.1. The assumption that there is no convective flow implies that the concentric fluid layers slide over each other. From equation 2.6, we can additionally derive the volumetric flow rate, Q and the average velocity, $\overline{u_z}$ as,

$$Q = -\frac{\pi R^4}{8\eta} \frac{\partial P}{\partial z} \quad \dots(2.7)$$

$$\overline{u_z} = \left(-\frac{\partial P}{\partial z}\right) \frac{R^2}{8\eta} \quad \dots(2.8)$$

Equation 2.7 provides a nice method to check and troubleshoot our fluid flow, by comparing the estimated value of Q with that measured by the flow sensor. A discrepancy between these values indicates either a blockage in the channel, or a leakage of the liquid.

2.4 Modelling the streaming current for non-ideal surfaces

We wish to understand and model the modified streaming current upon surface attachment of particles on the sensor surface. This is necessary to predict

the evolution of the streaming current as the surface evolves from ideally smooth to a rough, particle covered surface. Note that we use the general term ‘particle’ here as the model is not restricted to proteins or vesicles. Obtaining an expression for the streaming current in the presence of adsorbed particles requires solving the modified versions of both of the Navier-Stokes and Poisson-Boltzmann equations. In this situation, these equations become considerably complex and there is no known exact analytical solution [33], [34]. However, solutions under various limiting cases do exist in literature. Hayes and coworkers have tackled the problem with an empirical solution based on their experiments with a certain degree of accuracy [35]–[37]. Adamczyk et. al. however have developed numerical solutions that hold over a wider range of parameters and have verified them with experiments [34], [36], [38]–[40]. We hence adopted this solution for our case, and have tested them against measurements with various proteins in chapter 3. The modified streaming current for a particle covered surface is then given by [34], [38]:

$$I_S = I_{S0} \left(1 - A_i \theta + \frac{\zeta_p}{\zeta_i} A_p \theta \right) \quad \dots(2.9)$$

where I_{S0} is the initial streaming current of the bare sensor surface before the particle binding, θ is the portion of the sensor surface covered by the bound particles, ζ_p is the zeta potential of the particle, and ζ_i is the zeta potential of the bare sensor surface. Furthermore, we have the expressions of A_i and A_p as

$$\begin{aligned} A_i &= \frac{1 - \exp(-C_i \theta)}{\theta} \\ A_p &= \frac{1 - \exp(-C_p \theta)}{\theta}. \end{aligned} \quad \dots(2.10)$$

Here, C_i and C_p refer to perturbation in the macroscopic flow and electrical charge density due to the adsorbed particles on the sensor surface. These parameters are functions of the normalized radius, $a_r = \frac{a}{\lambda}$, where a is the hydrodynamic radius of the particle, and λ is the Debye length. The flow perturbation is due to the size of the particles, whereas the electrical charge density perturbation is due to their charge. Moreover, in the limit of low θ , $A_i = C_i(\theta)$ and $A_p = C_p(\theta)$, and equation 2.2 reduces to:

$$I_S = I_{S0} \left(1 - C_i \theta + \frac{\zeta_p}{\zeta_i} C_p \theta \right) \quad \dots(2.11)$$

It is worthwhile to mention as well that this model assumes the length scale of the variation in the shear rate has to be much larger than that of the particle dimensions, but is otherwise valid for an arbitrary shear flow.

The dependence of C_i and C_p on a_r was calculated numerically by Adamczyk et. al. [34] by solving the Navier-Stokes and Poisson-Boltzmann equations at the interface using a bispherical coordinate system, and the solution is plotted in figure 2.6. In the range $2 < a_r < \infty$, the values of C_i and C_p remain nearly unchanged. In the limiting case of $a_r \gg 1$, C_i approaches the value 10.21, while C_p approaches 6.51. On the other hand, in the range of relatively thick Debye length, i.e. $a_r < 2$, C_i decreases whereas C_p increases.

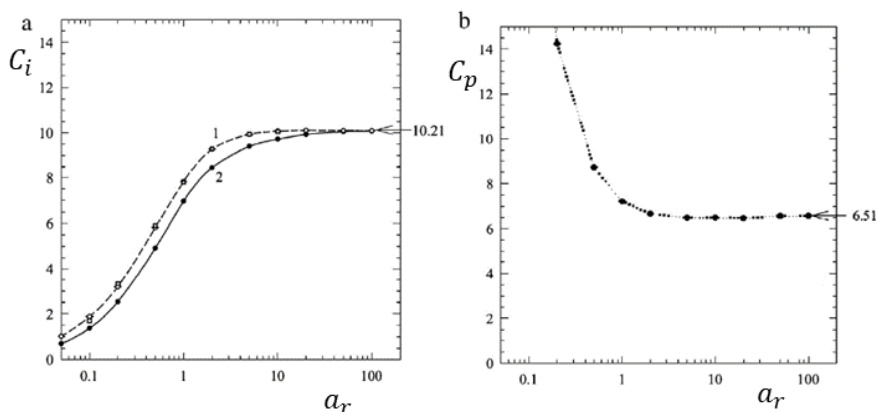


Figure 2.7. The dependence of the parameters (a) C_i and (b) C_p on the normalized radius, a_r , calculated using numerical simulations. Figures adapted with permission from ref. [34]. © 2009 Elsevier B.V.

2.5 Hydrodynamic radii of proteins

The estimation of the radii of proteins in the measurement buffer followed the result that the partial volume, v_2 of most proteins lie in a narrow range of 0.70 to 0.76 cm³/g and can be assumed to have an average value of 0.73 cm³/g [41]. One can then obtain a direct relation between the measured molar mass of the proteins and the volume it occupies in the buffer. For these calculations, we assume for simplicity that the protein tends to be globular rather than elongated in the PBS buffer. Hence, monomeric proteins are assumed to be spherical, whereas dimeric proteins are assumed to be two spheres joined together. The relationship between the volume, V in nm³ and the molar mass, M in Da (dalton) is given by:

$$V = \frac{v_2 c}{N_A} M \quad \dots(2.12)$$

where, $N_A = 6.023 \times 10^{23}$ is Avogadro's number, and $c = 10^{21} \text{ nm}^3/\text{cm}^3$ is the conversion factor. The radius can then be calculated using either $V = \left(\frac{4}{3}\right) \pi a^3$ or $V = \left(\frac{8}{3}\right) \pi a^3$, with a being the radius, depending on whether the protein is a monomer or dimer. The hydrodynamic radii for a monomer is then given by $R_H = a$, while that for a dimer is given by $R_H = 1.39a$ [34].

2.6 Electrophoretic light scattering (ELS)

The molecular zeta potential, ζ_p values of the various proteins used were determined using ELS [42] (Delsa™ Nano C, Beckman Coulter). This method involves first estimating the diffusion coefficient of the protein from its Brownian motion using light scattering. The diffusion constant, D is given by:

$$D = \frac{\langle \overline{x, y}^2 \rangle}{4t} \quad \dots(2.13)$$

where $\langle \overline{x, y}^2 \rangle$ represents the mean squared displacement in two dimensions in the time interval, t . The radius, a of the protein is then estimated using the Stokes-Einstein relation:

$$D = \frac{k_B T}{6\pi\eta a} \quad \dots(2.14)$$

where k_B is the Boltzmann constant, T is the temperature and η is the dynamic viscosity of the medium. The electrophoretic mobility can be estimated from the relation $\mu_E = v/E$, where v is the velocity of the protein under the applied electric field, E . ζ_p is then calculated from the Helmholtz-Smoluchowski equation:

$$\zeta_p = \frac{4\pi\eta}{\epsilon} f(\lambda) \mu_E \quad \dots(2.15)$$

where, $f(\lambda)$ is the Henry function.

2.7 Extracellular vesicles: what makes them particularly suitable targets for our sensor?

In the latter parts of the thesis, we shall focus extensively on the detection and surface protein profiling of extracellular vesicles (sEVs), discuss and compare a few surface functionalization strategies from the point of view of the surface charge of the sensor. Before discussing what makes our sensing method particularly sensitive to sEVs, let's discuss their biological and clinical significance. These nanovesicles are released by almost all cell types, and are used for inter-cellular communication [43]. They are quite heterogeneous in their biophysical properties such as their size [44], charge [43], Young's modulus, [44] and expression of surface proteins [45], [46]. There has been tremendous research interest towards sEVs after the discovery that they are potential sources of biomarkers for various types of cancer [47]. Hence, they have recently attracted considerable research interest for diagnosis and treatment of various types of cancer [45], [48]–[50].

Even though sEVs are quite heterogeneous, they are typically quite larger in size than the Debye length of our biosensor in 0.1x PBS buffer that we use during the measurements (λ for 0.1x PBS is 2.3 nm). sEVs normally lie in the range of 40 – 200 nm in diameter [51]. Moreover, they bear strong negative charge at the measurement pH (7.4) chosen to mimic physiological conditions. This is due to deprotonated COO^- groups, acidic sugars and other molecules on their surface [43]. Their molecular zeta potential is typically in the range -30 to -50 mV in PBS [43]. This means that their capture on the sensor surface causes perturbation not only in the flow profile, but also in the electrostatic charge density of the surface. As we shall discuss in chapter 3, both of these factors lead to a large signal. Yet another advantage is that, depending on the choice of the capture probe used, there may be several binding sites on the surface of the sEVs, corresponding to the amount of the targeted surface proteins. This not only increases the probability of capture of the sEVs, but also opens up the possibility to profile the expression level of a surface protein of the captured sEVs with a detection probe. The larger diameter of the sEVs however decreases the diffusion constant of the sEVs. The injection time of the sEVs thus has to be longer in order to let the sensor surface attain a steady state, in comparison to using a target with smaller diameter, such as most proteins.

2.8 How do we express the signal?

All our sensing measurements involved measuring the streaming current. However, the signal was reported in terms of the zeta potential rather than the streaming current throughout the thesis. The reason is that the zeta potential is

a surface property of the sensor that is independent of the channel dimensions and the applied pressure. So it is easier to compare the signal across various measurements even if these parameters were different. The zeta potential of the sensor surface (ζ) is related to I_S via the relation [52]:

$$\zeta = \frac{\Delta I_S}{\Delta P} \frac{\eta}{\epsilon_r \epsilon_0} \frac{L}{A} \quad \dots(2.16)$$

Here, $\frac{\Delta I_S}{\Delta P}$ is the slope of the streaming current vs. pressure plot, η is the dynamic viscosity of the medium, $\epsilon_r \epsilon_0$ is the permittivity of the electrolyte used, and L and A are the length and area of cross section of the channel used. Equation 2.16 can be derived from equation 2.2 and 2.6 and from the fact that for a cylindrical channel, the streaming current is given by $\Delta I_S = 2\pi \int_0^R u_z(r) \rho_E(r) dr$, with R being the radius of the channel. It is important to note that the above definition of the zeta potential holds for an ideally smooth surface and uniform charge distribution [52]. Upon adsorption of the target on the sensor surface however, both the assumptions are no longer valid. Hence, we shall use the term apparent zeta potential (ζ^*) instead to refer to this quantity.

2.9 Differential measurement with trapezoidal pulses

An additional condition for equation 2.16 to be valid is that the plot of I_S vs. P must be linear [53]. This can however deviate from linearity because of several reasons such as faulty microfluidic connections, air bubbles and a chemically inhomogeneous surface. These connections can also malfunction after prolonged exposure to high pressures. Another endearing issue is the electrode drift, which can be rather high when the electrodes are not sufficiently clean, or if they get contaminated during the measurement. Using a trapezoidal pressure pulse lets us monitor and troubleshoot both of these issues in real time. A plot of the trapezoidal pressure pulse and the resulting streaming current profile is shown in figure 2.8. The two pulses have a phase difference of π in this case as the surface has negative zeta potential. It can be clearly seen that during the linear portion of the pressure pulse, the streaming current also changes linearly. Ideally, in the absence of any surface adsorption, the streaming current should also maintain a constant value during the flat portion of the pressure pulse. However, this is not the case in figure 2.8 due to the electrical drift. It often suffices to wait until the drift becomes very small (0.05 mV/min or smaller). Otherwise, we carry out a thorough cleaning of the electrodes.

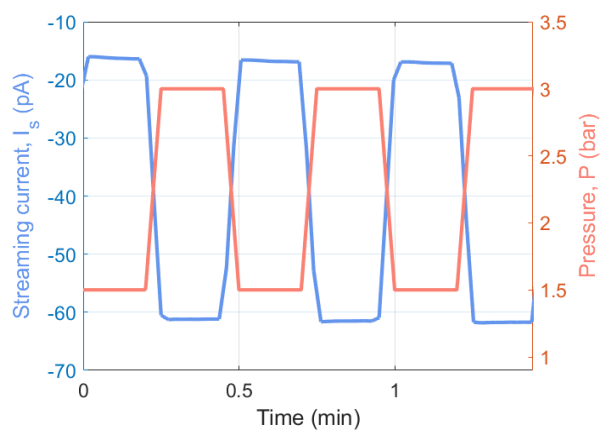


Figure 2.8: Differential measurement using trapezoidal pressure pulses, along with the resulting streaming current profile.

3. Influence of the size and charge of a target

In order to design a streaming current-based biosensor that can be potentially utilized to detect a wide variety of targets, it is vital to take into account how various physical properties of a target such its size and electrical charge can affect the signal. Theoretical models exist [34], [36], [38] that predict a dependence of the signal on the size, charge and shape of the target. However, experimental validation of these models are rare, and mostly concern larger, inorganic particles [38], [39], [54]. In the context of biosensing, the size range of $a \sim 1$ nm is significant as a lot of proteins and other biomolecules of diagnostic importance lie in this size range. An additional motivation to select this size range is to validate the theoretical predictions for sizes of the order of the Debye length ($\lambda = 2.3$ nm for 0.1x PBS). Moreover, the influence of molecular charge has not been adequately addressed in literature. In this chapter, we shall describe the influence of molecular size and charge on the signal generated by a set of engineered proteins. We shall start with the theoretical predictions, and examine the circumstances when the experimental results agree with the theory. We shall then proceed to understand those cases when the experiments do not agree with the theory, and if they can be reconciled by taking additional factors into consideration.

3.1 How does the binding of the target molecules modify the surface properties?

In order to model the sensor response as a function of the surface coverage of bound target molecules, e.g., proteins, we start with the expression of the modified streaming current for a particle covered surface, described in detail in section 2.2, given by:

$$I_S = I_{S0} \left(1 - A_i \theta + \frac{\zeta_p}{\zeta_i^*} A_p \theta \right) \quad \dots(3.1)$$

See section 2.2 for the description of the symbols in the above equation. We shall next proceed to adapt this model to our sensor. We begin by differentiating equation 3.1 with respect to P . We then have

$$\frac{dI_S}{dP} = \frac{dI_{S0}}{dP} \left(1 - A_i \theta + \frac{\zeta_p}{\zeta_i^*} A_p \theta \right) \quad \dots(3.2)$$

As we report the signal in terms of the zeta potential, it is more useful to re-write equation 3.2 making use of equation 2.16. We then have,

$$\begin{aligned} \zeta^* &= \zeta_i^* \left(1 - A_i \theta + \frac{\zeta_p}{\zeta_i^*} A_p \theta \right) \\ \Rightarrow \zeta^* &= \zeta_i^* (1 - A_i \theta) + \zeta_p A_p \theta \end{aligned}$$

Defining the net signal as $\Delta\zeta^* = \zeta^* - \zeta_i^*$ and substituting the expressions for A_i and A_p , we have,

$$\Delta\zeta^* = -\zeta_i^* (1 - \exp(-C_i \theta)) + \zeta_p (1 - \exp(-C_p \theta)) \quad \dots(3.3)$$

Equation 3.3 models the combined effect the hydrodynamic and electrostatic perturbation brought about by the bound target proteins. The values of C_i and C_p are estimated from numerical solutions to the Navier-Stokes and Poisson-Boltzmann equations [34]. These parameters are dimensionless functions of the normalized radius, a_r .

3.2 The model system

There are numerous challenges with investigating these theoretical predictions with biomolecules. First, we need a set of molecules where either the size or charge can be varied independent of each other. This is difficult to achieve in naturally occurring proteins. Secondly, affinity based capture may introduce substantial differences in the surface coverage, complicating the analysis. To mitigate these challenges, we used a set of synthetic molecules called affibodies, and also used an unbiased capturing strategy in order to design a reliable investigation of the influence of their size and charge on the overall signal. Affibodies are a class of synthetic proteins that mimic the function of antibodies [55]. Further, we could use the monomeric or dimeric forms of the affibodies, in order to vary their size. However, the results and interpretation are still qualitative in nature since it is almost impossible to design molecules that accurately fulfil the above-mentioned criteria. Four different affibodies were obtained from the same parental protein (7 kDa B-domain of the staphylococcal protein A), and the target specific binding surface had a variation of 13 amino acids. All the affibody domains used in this study had the same structure: rod-shaped three-helix-bundle. On the other hand, they had different amino acid

compositions in two of the helices. These affibodies were produced in monomeric and dimeric forms, allowing the investigation of seven distinct affibodies. Further details about the synthesis of the affibodies are described in ref. [53].

Our experiments involved a set of well characterized affibodies in the sub-Debye length size range ($a \sim 1$ to 2 nm), and two standard antibodies of slightly higher size range ($a \sim 3$ to 5 nm). Here, the values of a refer to the hydrodynamic radii, and their calculation is detailed in section 2.5. The molecular weights of the analytes were in the range of $9 - 460$ kDa. The range of the molecular charge, quantified by the molecular zeta potential, ζ_p was in the range ~ -9 to 20 mV. The detailed information of each of the analytes used is presented in table 3.1. Moreover, the capture of these analytes on the sensor surface followed a covalent binding strategy in order to remove the differences arising from affinity differences in affinity-based capture.

Table 3.1 Details of size and charge of the analytes studied: apparent molecular weights as measured by size exclusion chromatography (SEC), calculated hydrodynamic radii (a), normalized radii (a_r) and molecular zeta potential (ζ_p) as measured by ELS (see section 2.6 for details). Adapted with permission from Paper I [53]. © 2020 Elsevier B.V.

Protein	Construct	Symbol	Apparent molecular weight (kDa)	a (nm)	a_r	ζ_p (mV)
anti-HER3	Monomer	S1A	10.6 ± 0.1	1.5	0.62	-1.9 ± 0.3
anti-EGFR	Dimer	S2A	21.7 ± 0.6	2.0	0.87	-7.5 ± 0.9
anti-EB3	Monomer	S1B	11.1 ± 0.3	1.5	0.63	-8.7 ± 0.6
anti-EB3	Dimer	S2B	25.9 ± 0.1	2.2	0.92	-9.2 ± 0.7
anti-HER2	Monomer	N1	7.3 ± 0.3	1.3	0.55	0.2 ± 0.1
antiHER3	Dimer	N2	18.9 ± 0.4	1.9	0.83	0.3 ± 0.2
anti-HER2	Dimer	O2	14.0 ± 0.6	1.8	0.75	2.7 ± 0.3
Cetuximab	—	CET	193.4 ± 2.6	3.8	1.63	1.5 ± 0.5
C1Q	—	C1Q	460^a	5.1	2.18	19.6 ± 0.3

^aThis value has been obtained from literature [56]

3.3 Theoretical predictions

In order to understand the complex interplay of the size and charge of the target molecules in determining the net signal, we have to deal with both these aspects individually. For isolating the effect of the size, we can set $\zeta_p = 0$ in equation 3.3, representing charge-neutral particles, resulting in the expression,

$$\Delta\zeta^* = -\zeta_i^*(1 - \exp(-C_i\theta)) \quad \dots(3.4)$$

Equation 3.4 now deals with neutral target particles of radius a and surface coverage θ . For the sake of simplicity, we assume each particle to cover a surface area equivalent to a disc of radius a on the sensor surface. We then proceed to plot a 3D graph of $\Delta\zeta^*$ vs. a_r and θ , as shown in figure 3.1a. As the dependence of $\Delta\zeta^*$ on θ is exponential, it is approximately linear in the limit of small values of θ . On the other hand, the slope of $\Delta\zeta^*$ vs. a_r is large for smaller values of a_r and approaches zero at larger values of a_r . This implies that the sensor response changes more with the size of the target particles when it is of the order of λ . For a larger particle ($a_r \gg \lambda$) however, the sensor response changes less with the size of the particle. This aligns with the fact that the streaming current is an interface phenomenon, restricted largely within the electrical double layer.

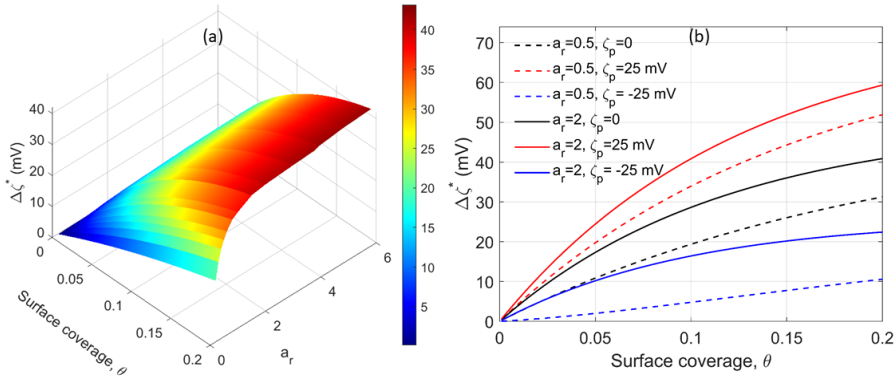


Figure 3.1. (a) Simulation of the sensor signal ($\Delta\zeta^*$) against the surface coverage θ and normalized radius a_r shown as a 3D plot. $\Delta\zeta^*$ increases with respect to a_r and begins to saturate for $a_r > 1$. (b) Simulations illustrating the influence of charge on the signal for $a_r = 0.5$ and 2 for various values of the molecular zeta potential, $\zeta_p = 25, 0$ and -25 mV. For each of these cases, ζ_i^* is assumed to be -50 mV and the values of C_i and C_p are taken from [34]. Image reproduced with permission from Paper I [53]. © 2020 Elsevier B.V.

How, and to what extent does the charge affect the signal? Proteins have amino acids that get ionized in a polar solvent, the extent of ionization being dependent on the pH [57]. This imparts them charge, which we quantify in terms of the molecular zeta potential, ζ_p . To understand the influence of this charge on the signal, we carried out simulations for two different sizes, with $a_r = 0.5$ and 2. Considering the sensor surface to be negatively charged, with $\zeta_i^* = -50$ mV, we considered three types of charged particles, corresponding to which, $\zeta_p = 25, 0$ and -25 mV. This selection allowed us to use the values of C_i and C_p which had been calculated earlier [34]. The results are plotted

in figure 3.1b. Clearly, the signal is the strongest when the proteins carry opposite charge relative to the sensor surface, and lowest when the sign of their charge is the same as that of the sensor surface. The simulations also predict that the signal is higher for larger analytes irrespective of their charge. The channel dimensions are large enough so that we could ignore the effects of solvent polarization [58] and steric hindrance [59] for these simulations.

3.4 Experimental validation of the simulations

The experimental investigations were performed using a commercial micro-capillary made of silica with an inner diameter of 25 μm . Surface functionalization was carried out on its inner surface, followed by fluidic and electrical measurements, the details of which are described below.

3.4.1 Surface functionalization

The first step of functionalization involved cleaning the capillary surface with a 5:1:1 ratio Milli-Q water, 25% NH_4OH and 30% H_2O_2 . This process involved dipping the capillary in glass vial containing the cleaning mixture, and securing it in place with the help of a septum in the cap of the vial as shown in figure 3.2. The vial was then placed on a heater at 88°C for 15 minutes. The heat drove the cleaning mixture through the capillary.

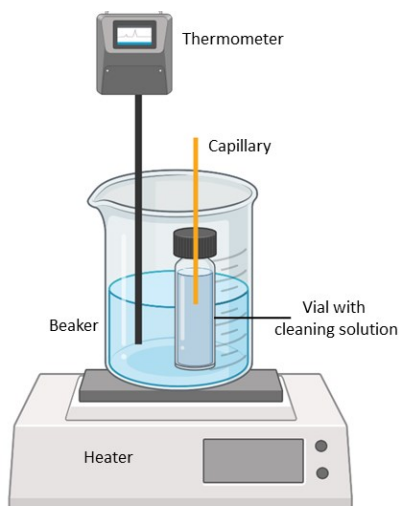


Figure 3.2. A schematic representation of the cleaning procedure followed for the capillary prior to the surface functionalization steps. Image created with BioRender.com

This process removes surface impurities and activates the hydroxyl groups. The cleaning step was followed by silanization with 5% w/v of (3-aminopropyl)triethoxy silane (hereafter called APTES) in 95% ethanol for 10 minutes. This was followed by immobilizing 1% glutaraldehyde (GA) for 1 hour, which serves to capture the analytes non-specifically via covalent linkage. The control measurements involved deactivation of the GA surface by flowing Tris-ethanolamine (0.1M Tris buffer and 50 nM ethanolamine, pH 9.0) blocking solution for 30 minutes before starting the measurements. All the connectors, tubes and the hollow platinum electrodes used in the measurements were passivated via treatment with 0.05% casein solution for 30 minutes before the start of the measurements.

3.4.2 Fluidic and electrical measurements

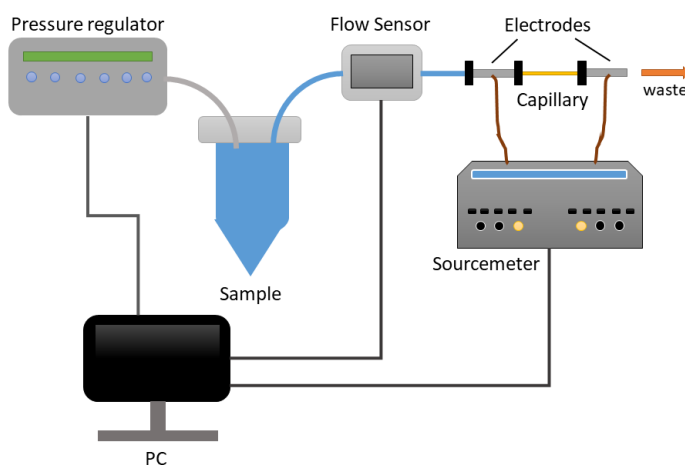


Figure 3.3. A schematic representation of the experimental setup showing the fluidic and electrical measurement apparatus. Image adapted with permission from Paper II [60] and partly created with BioRender.com. © 2020 Elsevier B.V.

A commercial pressure pump (OB1, Elveflow) was used for applying pressure across the capillary in order to flow the buffer and sample. A train of trapezoidal pressure pulses were generated for differential measurement, as detailed in section 2.9. The pressure was made to alternate between 1.5 and 3 bar. The resulting flow rate of the buffer was measured with the help of a flow sensor (MSF3, Elveflow). The streaming current generated as a result of the pressure-driven flow was measured by a sourcemeter (Keithley 2636A) via hollow platinum electrodes connected at the ends of the capillary. Baseline measurements involved measuring the ζ^* of the sensor surface while flowing $0.1 \times$ PBS before and after the analyte injection. The choice of the PBS buffer

(pH \sim 7.4) was motivated by the fact that it simulates physiological conditions quite well. The difference between the initial and final baseline was considered as the signal of the sensor for the analyte ($\Delta\zeta^* = \zeta_f^* - \zeta_i^*$). A schematic representation of the apparatus is shown in figure 3.3.

3.4.3 How well do the results agree with simulations?

An example of a typical real-time measurement is shown in figure 3.4a, for the case of the affibody N2. Both the initial and final baselines were measured and it was ensured that they were stable, with minimal drift. During the sample injection, the arrival of the sample plug at the capillary channel lead to an immediate drop in the signal, followed by a slow increase. The opposite response was recorded when the sample plug was replaced by the buffer plug. This sudden jump in the signal in response to sample injection is a common phenomenon in biosensing and is widely attributed to bulk composition effects [61]. A net increase in the ζ^* , representing the signal, $\Delta\zeta^*$ can be observed between the two buffer plugs. The start and end of the injection are marked by arrows. The initial baseline in all the cases was $\zeta_i^* = -34 \pm 2$ mV, and the final baseline either increased or decreased from this value.

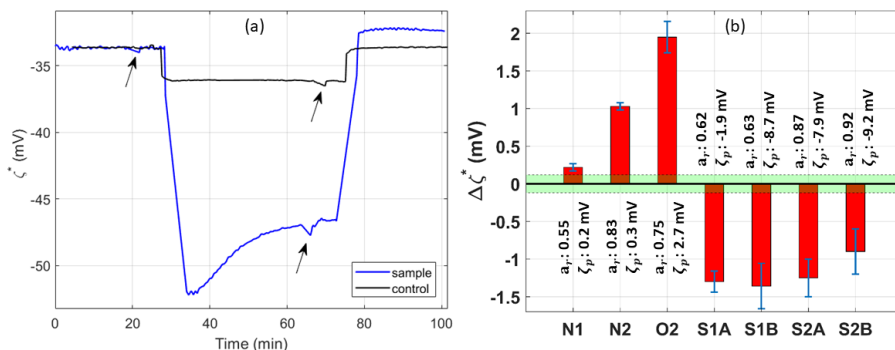


Figure 3.4 (a) Real-time sensor response to the binding of the affibody N2 and the corresponding control measurement. The beginning and end of the injection is indicated by arrows. The signal ($\Delta\zeta^*$) is defined as the difference between the initial and final baselines. (b) Bar plots comparing the signal from affibodies of various types of charge: neutral (N1 and N2), positive (O2) and negative (S1A, S1B, S2A and S2B). The values of a_r and ζ_p of each affibody is mentioned adjacent to its corresponding bar plot. The shaded area refers to the minimum detectable signal of 0.1 mV. Image reproduced with permission from Paper I [53]. © 2020 Elsevier B.V.

The signals of all the affibodies investigated have been summarized as bar plots in figure 3.4b. The height of each bar plot represents $\Delta\zeta^*$ and their direction represents whether the net change in the baseline as a result of the affibody binding was positive or negative. Each result has been control subtracted, and presented as an average, along with the standard deviation (SD)

over triplicate measurements. For convenience, the affibodies were grouped into three categories: (i) nearly charge neutral affibodies ($\zeta_p \sim 0$) under the experimental conditions (set N, monomeric affibody N1 and dimeric affibody N2), (ii) affibodies carrying opposite charge type ($\zeta_p > 0$) with respect to that of ζ_i^* (set O, dimeric affibody O2), and (iii) affibodies carrying the same charge type ($\zeta_p < 0$) as compared to that of ζ_i^* (set S, monomeric affibodies S1A and S1B, and dimeric affibodies S2A and S2B). The values of a of the proteins were estimated using the method described in section 2.5.

Let us now consider the signals generated by N1 and N2. Both are nearly neutral affibodies with their ζ_p being about 0.2 and 0.3 mV respectively in $0.1 \times$ PBS. The average signal corresponding to N2 is about five times that of N1. Furthermore, both N1 and N2 lead to an increase in the value of ζ^* , i.e., $\Delta\zeta^* > 0$ in both cases. As the overall sign of ζ^* is negative, this means that $|\zeta_f| < |\zeta_i^*|$, i.e. the magnitude of the surface zeta potential drops as a result of the affibody binding. This can be intuitively explained on the basis of additional impedance induced to stream of the ions in the EDL by the affibodies due to their size [54]. It is also important to note that even though N1 and N2 are nearly neutral, they can still provide small electrostatic perturbation due to the difference in the permittivity between the affibody and the sensor surface. Moreover, the small difference in their ζ_p values can contribute to the difference in the signal induced by them. The results are consistent with the predictions from simulations. A similar size dependence has also been observed for colloidal particles, due to a damping of the convection current of ions in the vicinity of the adsorbed particles [54]. This size dependence is expected to saturate however, as the analyte size becomes very large relative to the Debye length, as shown in figure 3.1a.

To study the case of affibody carrying opposite charge as compared to the surface, we compared the signals corresponding to O2 and N2. Each O2 molecule carries an overall positive charge, corresponding to a ζ_p value of 2.7 mV, with its radius being slightly smaller as compared to that of N2. We see that O2 not only induces a signal of ~ 2.0 mV, which is about twice the signal induced by N2, this signal is also the highest among all the dimeric affibodies tested. Hence, this case is also consistent with the theoretical predictions. On the other hand, the surprising results were obtained for the set of affibodies with same charges as the surface. The affibody set S1A, S2A, S1B, S2B are all negatively charged, $\zeta_p < 0$. Unlike the previous two cases, the sign of the signal is in fact negative, i.e. $\Delta\zeta^* < 0$ for this set of affibodies. Moreover, the signal for the dimeric affibody S2A is not very different from those of S1A and S1B, despite the differences in their size. Furthermore, the larger magnitude of ζ_p of S2A (-7.5 mV) in comparison to S1A (-1.9 mV) also does not apparently have any major influence on the signal. In addition, despite S2B

having largest size and magnitude of ζ_p , it induced the weakest signal among all the affibodies in the set. Both of these aspects are clear departures from the theoretical predictions that state that the signal is higher for larger sized molecules regardless the charge type, and that the net signal is positive even for negatively charged analytes. This apparent discrepancy between the results and the theoretical predictions were further examined in the next section.

3.5 A closer look at the apparent discrepancy

As described above, the theoretical predictions and the experimental results have a good qualitative agreement when the surface bound analytes are either nearly neutral, or have the opposite kind of charge as compared to the sensor surface. There is however an apparent discrepancy between the theoretical predictions and the experimental results obtained for the case of negatively charged analytes bound on a negatively charged surface. We first direct our focus on the fact that the signal inverts its sign for the negatively charged affibodies. To determine if such a situation is permissible within the framework of the model being used here, we plotted the signal $\Delta\zeta^*$ as a function of the parameter C_i , as shown in figure 3.5a for two cases i.e. $\zeta_p < 0$ and $\zeta_p > 0$. We discussed in section 2.4 about the numerical solutions that govern the values of C_i as a function of a_r . According to these solutions C_i increases with a_r for $0 < a_r < 2$, and attains saturation at the value of 10.21 for larger values of a_r . So we considered the range from 0 to 10.21 for the plot of $\Delta\zeta^*$ against a_r . As can be seen in the plot, the sign of $\Delta\zeta^*$ does indeed invert when C_i goes below a particular value. In contrast, for $\zeta_p > 0$ the sign of $\Delta\zeta^*$ does not invert for this range of values of C_i .

Having shown that it is within the framework of the model for the sign of $\Delta\zeta^*$ to invert for $\zeta_p < 0$, we repeated the simulation of $\Delta\zeta^*$ vs. θ for the same set of parameters as those presented in figure 3.1b, but with lower values of the parameter C_i . In particular, we used the values of C_i to be 5 and 10 times lower for the smaller ($a_r = 0.5$) and larger ($a_r = 2$) analytes respectively, than those extracted from simulations in figure 2.7. The results are plotted in figure 3.5b. Clearly, the trends are now consistent with the experimental observations. The overall signal is now lower in all cases as compared to the signal predicted in the previous set of simulations. The trends remain qualitatively unchanged for the analytes that are positively charged or are charge neutral. However, for the negatively charged analytes, the predictions are now remarkably different. Not only is the sign of the $\Delta\zeta^*$ now inverted, the larger analyte is also predicted to induce a weaker signal in comparison to the smaller one. This matches with the results in case of the affibodies S1B and S2B, where both have similar values of ζ_p , but S2B being the dimeric affibody, has a larger

hydrodynamic radius as compared to S1B. We must emphasize here that the results were qualitatively similar for a range of different values of C_i . The choice of C_i values for the plots in figure 3.5b was done only for a better illustration of the claim about the trends. A lower value of C_i has also been used to explain the experimental observations in another investigation involving nanoparticles [36]. We believe the physical explanation for this is that the functionalized surface already has some roughness to begin with, which is of the order of the hydrodynamic radii of the analytes used in this study. Such a roughness already causes some perturbation to the flow even before the analytes bind. This reduces the additional perturbation to the flow brought about by the binding of the analytes than what would be obtained if the surface were ideally flat to begin with.

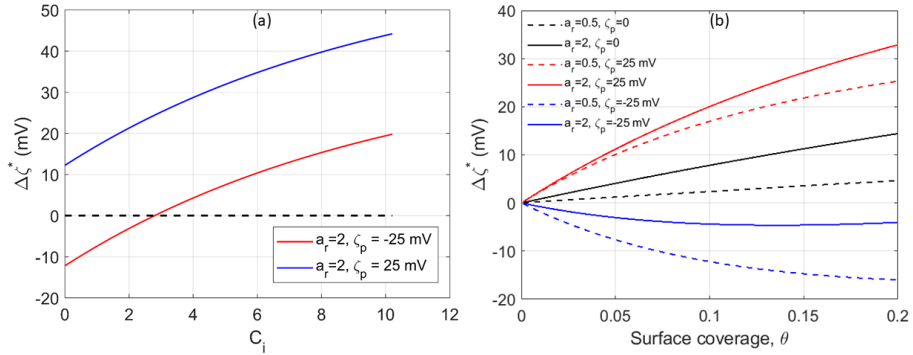


Figure 3.5 (a) $\Delta\zeta^*$ as a function of C_i for $a_r = 2$ and $\zeta_p = \pm 25$ mV. The plot shows that there exist a range of values of C_i , for which the sign of $\Delta\zeta^*$ inverts. (b) $\Delta\zeta^*$ vs. θ for $a_r = 0.5$ and 2, and $\zeta_p = 25, 0$ and -25 mV, but with smaller values of C_i than those extracted from simulations (figure 2.7). Image adapted with permission from Paper I [53]. © 2020 Elsevier B.V.

3.6 Modulating the signal via pH

In order to get a further insight into the size and charge dependence of $\Delta\zeta^*$, we decided to check the sensor responses to the nearly neutral affibodies N1 and N2, at different pH values of the measurement buffer. This would lead to a change in their net charge, while their size remained constant. For these measurements, the pH of the PBS buffer was changed to 6.4 and 8.4 in two separate cases. This led to a modulation in the ζ_p values of N1 and N2 from positive to negative values, which were measured using ELS, and are presented in figure 3.6a. It is vital to point out that the pH of the buffer was changed only during the measurement of the initial and final baselines, and not during injection of the affibodies, which were still carried out at a pH of 7.4. This was done to maintain identical conditions as in section 3.4.3 so that the binding of the affibodies to the surface is not affected by the pH. Another

important aspect is that the pH also affects the initial baseline, ζ_i^* and this can influence the generated signal. Hence, we also measured ζ_i^* as a function of pH in order to gauge this influence, as shown in figure 3.6b. We observed that the ζ_i^* of the surface remained abundantly negative, and changed from -31.5 to -36 mV when the pH changed from 6.4 to 8.4.

Having checked how the change of pH affects the values of ζ_p and ζ_i^* , two important parameters in equation 3.3, we can now focus on understanding how the overall signal varies with pH. The $\Delta\zeta^*$ induced by N1 and N2 for these pH dependent measurements are shown in figure 3.6c and 3.6d. It can be clearly seen that as the ζ_p of N1 changes from 0.7 to -0.8 mV, the value of $\Delta\zeta^*$ responds accordingly, indicating the influence of electric charge. A similar trend was observed for the dimer N2. In particular, when $\zeta_p > 0$, the signal $\Delta\zeta^*$ corresponding to both N1 and N2 is positive, with N2 inducing a stronger signal. As ζ_p approaches 0, $\Delta\zeta^*$ falls for both. Lastly, as ζ_p becomes negative, the value of $\Delta\zeta^*$ inverts for both N1 and N2. However, even though ζ_p was varied approximately to the same extent on both sides of the neutral condition, change in the signal induced by N1 and N2 corresponding to these values were quite different. While N1 induced similar signal for both positive and negative ζ_p , in case of N2, the signal for positive ζ_p was about six times the signal corresponding to negative ζ_p . All of these aspects agree very well with the theoretical analysis presented in section 3.5.

It is important to point out that the signal enhancement as shown in figure 3.6b and 3.6c is not entirely due to modulation of ζ_p with pH. The parameter ζ_i^* also responds to pH, and according to equation 3.3, this should also have a contribution to the signal. To understand and visualize how significant this contribution is, we plotted $\Delta\zeta^*$ as a function of ζ_i^* for both the monomeric and dimeric case, as shown in figure 3.7a. As ζ_i^* varied from -31.5 to -36 mV in the measurements, we chose this range for the plot. Moreover, as described in section 3.5, the influence of the surface roughness was accounted for by choosing the values of C_i to be 0.49 and 1.70 for the monomeric and dimeric cases respectively. As shown in figure 3.7a, the value of $\Delta\zeta^*$ changes by 0.18 and 0.38 mV respectively as ζ_i^* changes from -31.5 to -36 mV. In comparison, the change in $\Delta\zeta^*$ observed experimentally for N1 and N2 were 1.4 and 1.9 mV respectively. Hence, the influence of ζ_i^* contributes to only about $1/6^{\text{th}}$ of the overall change in the $\Delta\zeta^*$ as a result of the pH change. This is essentially due to fact that the parameter C_i is much smaller than C_p for $a_r < 1$. Furthermore, the initial surface roughness further reduces the influence of C_i . It is known that the with the rise of the surface roughness, the streaming current decreases [34]. Practically, the case of there being some initial surface roughness is similar to the situation of proteins binding to an ideally smooth surface with $\zeta_p = \zeta_i^*$. In either case, there is dampening of convection currents from ions close to the surface. Thus, when molecules with size comparable to the

surface roughness bind, the flow perturbation is expected to be weaker, effectively diminishing the influence of C_i .

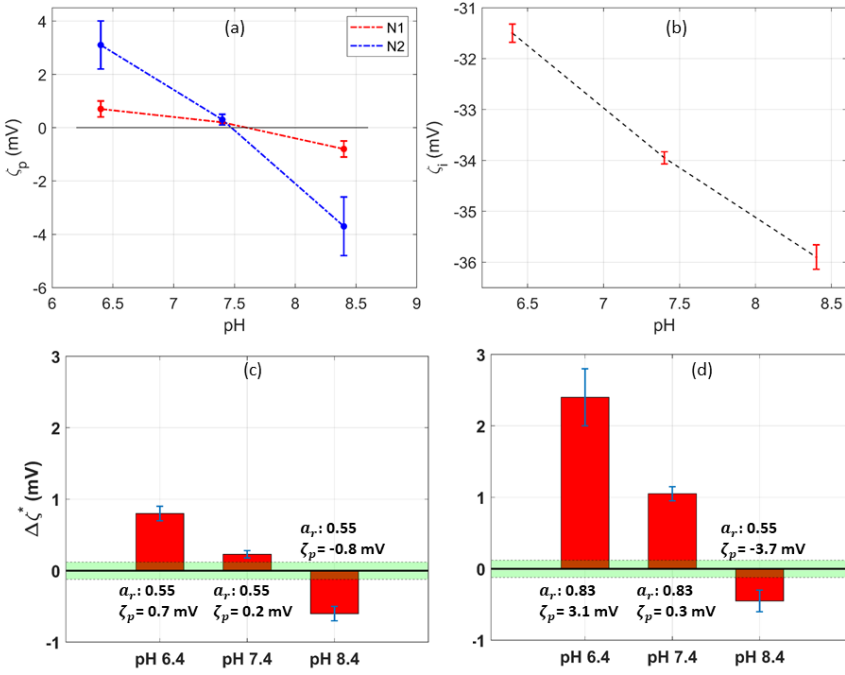


Figure 3.6. Demonstration of signal enhancement with pH. Changing the pH from 6.4 to 8.4 leads to change in the values of (a) ζ_p of N1 and N2, as well as (b) ζ_i^* of the capillary surface. The resulting signals for these pH values for the affibodies (c) N1 and (d) N2 show a clear dependence with pH. These are in good agreement with the theoretical predictions in the section 3.5. Image reproduced with permission from Paper I [53]. © 2020 Elsevier B.V.

3.7 Does the sensor have a unique limit of detection?

As the preceding sections show, the sensor response clearly depends on the size and charge of an analyte. The sensor is hence expected to have a different limit of detection (LOD) for different analytes. But how large can this difference be? To evaluate this, we selected three analytes: the affibody O2, antibody CET, and complementary component C1Q. Among these, C1Q has the largest size and charge parameters ($a_r = 2.2$; $\zeta_p = 19.6$ mV), followed by CET ($a_r = 1.6$; $\zeta_p = 1.5$ mV), while O2 had the smallest size and intermediate charge ($a_r = 0.8$; $\zeta_p = 2.7$ mV). The concentration dependent response of the sensor is presented as semi-logarithmic plots in figure 3.7b. To

compare the sensor responses, we define the term sensitivity S_i as the minimum concentration of the analyte that produces a signal equal to the noise floor ($3 \times \text{SD}$ of the initial baseline). We estimated this concentration from an exponential fit of the signal vs. concentration curve. The strongest signal was generated by C1Q, followed by CET and O2. The values of S_i for C1Q CET and O2 were 0.26, 3.75 and 69.24 nM respectively. C1Q is thus 14-fold more sensitive in comparison to CET, and a 266-fold more sensitive as compared to O2. It is vital to point out that the term sensitivity is not used in a conventional sense here, as it is normally used to refer to specific and reversible interactions with affinity reagents. We instead captured the analytes covalently throughout this study in order to avoid the effects on the signal arising from differences in affinity. The analytes hence underwent random sequential adsorption for a time-limited injection (40 minutes).

The two orders of magnitude disparity in the sensitivity between O2 and C1Q shows the extent to which the sensor response can vary depending on the physical properties of the analyte. The same observation holds for the analytes under different pH, as observed for N1 and N2. Although this study only involved non-specific binding, the results can be extended to specific bio-detection as well. The vast majority of literature usually quotes a single value for the limit of detection (LOD) of a sensor. However, our results indicate that the LOD of a sensor is not always a unique number and may depend on the properties of the analyte being detected.

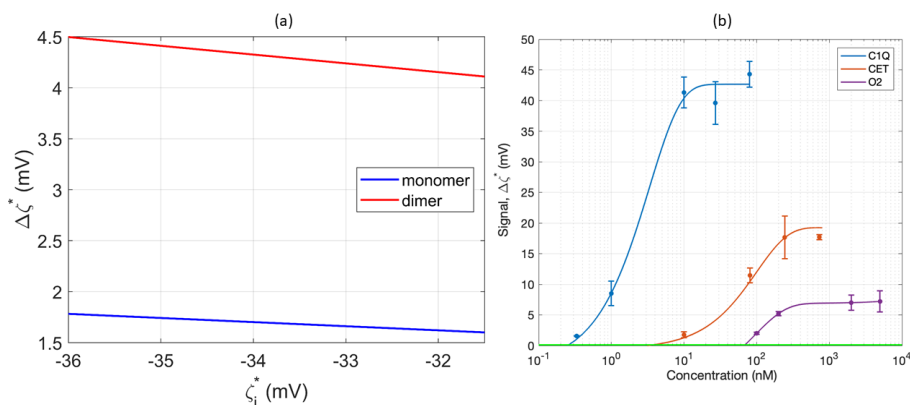


Figure 3.7 (a) Dependence of the signal ($\Delta\zeta^*$) on the baseline surface zeta potential (ζ_i^*) for the affibodies N1 and N2. (b) Concentration dependent signal for C1Q, CET and O2. As C1Q has larger size as well as larger positive charge, it induced a larger signal as compared to CET and O2. S_i values for C1Q, CET and O2 were 0.26, 3.75 and 69.24 nM respectively. Image reproduced with permission from Paper I [53]. © 2020 Elsevier B.V.

3.8 Chapter Summary

Molecular size and zeta potential were thus shown to be critical parameters in determining the overall signal in streaming current measurements. Analysis with both theoretical methods, using an established model, as well as experimental measurements using a set of well characterized proteins demonstrate this dependence. The experimental results were in good qualitative agreement with the theoretical predictions, and show that the sensor response increased with molecular size and zeta potential when the proteins carried a net positive charge. The dependence was similar for proteins that were nearly neutral. However, for negatively charged proteins, the dependence with size gradually saturated as the diameter exceeded the Debye screening length of the electrolyte. We expect this to be true for the positively charged proteins as well, although we did not observe it for the range of sizes we could test with the chosen protein set. There was also an apparent departure from the theoretical predictions when the conjunction of proteins carrying the same type of charge as the surface showed little to no dependence on the molecular size and zeta potential. This discrepancy could be explained within the framework of the same theoretical model, but by taking into account a stronger influence of the surface roughness. This chapter further shows that the sensitivity of the sensor can vary over several orders of magnitude as a result of the differences in the molecular size and zeta potential. These results can hence be useful in analysing the signal of a variety of molecules and devising strategies to enhance the signal induced by them.

4. Improving Sensitivity by Surface Charge Optimization

4.1 Signal enhancement in surface based sensors

A key factor to consider for any biosensing method is its sensitivity. Various methods have been explored in order to enhance the sensitivity of surface based biosensors, such as surface engineering [62], [63] and innovative electrode designs [64], [65]. Another approach is to optimize the surface functionalization strategy in order to increase the capture efficiency/density. Various surface functionalization protocols have been developed for different applications [66]–[68]. As presented in the previous chapter, the detection sensitivity of the streaming current-based method is strongly influenced by the charge of an analyte. So the obvious next question is; how do the electrical properties of surface influence the sensor response? Is it possible to modulate these properties to achieve a better sensitivity?

In this chapter, we examine the electrostatic properties of functionalized surfaces and their influence on the sensor response. We compared three different functionalization strategies altering the zeta potential of the functionalized surface in the range -16.0 to -32.8 mV. For this investigation, sEVs derived from non-small cell lung cancer cell line (NSCLC, H1975) were used as the target. The detection sensitivity, measured in terms of LOD, was found to vary over two orders of magnitude depending on the choice of surface functionalization strategy. The optimized functionalization method was then used to study the prospect of monitoring the effectiveness of targeted cancer therapies in a model lung cancer cell line (H1975) by analysing sEVs collected from the cells upon treatment with different cancer medicines. Further, the method was applied to analyse clinical sEVs derived from pleural effusion of NSCLC adenocarcinoma patients with smaller sample volumes as compared to previous approach with the same method.

4.2 Experimental setup

The electrical and fluidic measurements were performed similarly as described in chapter 3. However, a key difference is that the measurements were multiplexed rather than using a single channel. Prior to the measurements, the

connecting tubes as well as the hollow Pt. electrodes were treated for NSB. An illustration of the setup is shown in figure 4.1. Further description of the multiplexed setup is found in a separate article [69]. Multiplexing the method significantly reduced the time needed for multi-marker analysis.

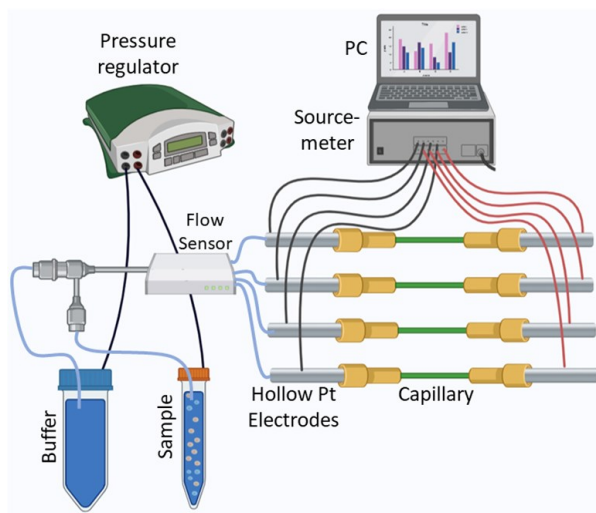


Figure 4.1: A schematic illustration of the multiplexed setup used in this study for the electrical and flow measurements. Image adapted from Paper II [70] with permission from ACS Publications, licensed under CC BY 4.0.

4.3 Surface functionalization strategies

4.3.1 Protocol details

Three different functionalization approaches were tested in this study. These three approaches were selected based on the extent of surface charge modulation that could be achieved with them, allowing us to gauge its influence on the signal. These approaches included the previously used covalent approach [51] involving APTES and GA, which have been described in chapter 3 and 5; and a non-covalent functionalization approach involving poly-L-lysine (PLL). PLL can be purchased commercially, and has been well characterized [71], [72]. We used a copolymer of PLL grafted with biotinylated polyethylene glycol (PEG), hereafter referred to as PPB. The PEG serves to reduce the non-specific binding [73], whereas the biotin was conjugated to a linker (either avidin or streptavidin, both of which have four binding sites available for biotin) in order to immobilize the capture probe.

- i. *Approach 1 (PPB-avidin)*: PPB was attached to the silica surface of the sensor via surface adsorption by flowing 0.1 mg/mL solution of

PLL in Milli-Q water for 30 min. The surface adsorption proceeded via electrostatic interaction between the negatively charged silica surface and the positively charged PLL backbone of the copolymer. This was followed by conjugation of avidin to the biotin terminal of the PPB by flowing a solution of 1 μ M solution of avidin in 1x PBS for 30 min.

- ii. *Approach 2 (PPB-streptavidin)*: Streptavidin was used instead of avidin in this approach. Everything else, including the concentrations and immobilization durations were kept the same.
- iii. *Approach 3 (APTES-GA)*: This approach has been described in detail in chapter 5. It involves a self-assembled monolayer of APTES and using GA as the linker. It is the standard functionalization method used in our previous studies on sEV detection using the streaming current method.

The above functionalization steps were followed by the immobilization of the capture probes. In case of PPB-avidin/streptavidin, the biotinylated versions of the capture probes were used in order to conjugate them to the avidin/streptavidin layer whereas in case of APTES-GA, the capture probes were directly conjugated to the surface. An illustration of these functionalization approaches is given in figure 4.2. It is important to point out that water was chosen as the solvent for PPB. The reason was that PPB layer links to silica via electrostatic attraction as they have opposite charges and we wanted to minimize the Coulomb screening.

4.3.2 Non-specific binding (NSB) and negative control

As this is a major concern in any sensing method, special attention needs to be paid to reduce NSB. In case of PPB-avidin/streptavidin, NSB was reduced to some extent by the PEG component of the PPB copolymers. However, this alone was not sufficient, as there was still a significantly large NSB of the sEVs with the surface (data not shown), likely due to the avidin layer. In order to further reduce NSB, the surface was treated with pluronic (synperonic) F108 solution for 15 min, which is non-ionic in nature. We did not use casein in this approach as it bears a strong negative charge and masked the positive charges that would hamper our desired extent of surface charge modulation. In case of the APTES-GA approach however, we used the aldehyde group deactivation via Tris-ethanolamine and the casein blocking as described in detail in chapter 5. The negative control measurements were performed using mouse IgG1 (IC002B, Bio-Techne) isotype control antibodies.

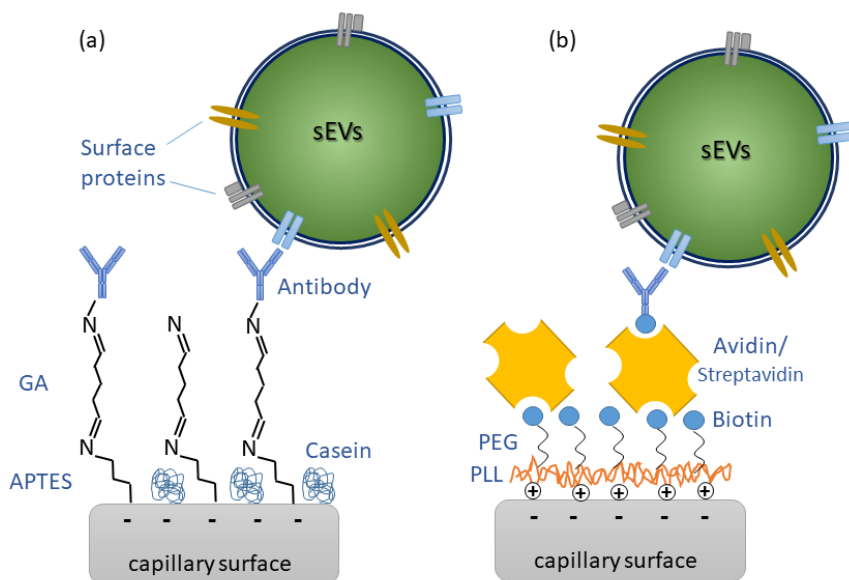


Figure 4.2: An illustration of the different functionalization approaches used for the surface charge modulation: (a) APTES-GA: this involved immobilizing the capillary surface with a self-assembled monolayer of APTES, followed by a GA linker, in order to link it with the capture probes. (b) PPB-avidin/streptavidin: the capillary surface was coated with a layer of PPB, followed by either an avidin or a streptavidin linker, which was further linked to a biotinylated version of the capture probe. Image adapted from Paper II [70] with permission from ACS Publications, licensed under CC BY 4.0.

4.3.3 Initial zeta potential of the surface and signal enhancement

The baseline measurements were performed similar to that described in chapter 3. The initial and final baselines were measured in 0.1x PBS whereas the sample injection was done in 1x PBS. The three different functionalization approaches led to three different corresponding values of the initial surface zeta potential (ζ_i^*). The PPB-avidin functionalization resulted in the highest (least negative) value of $\zeta_i^* = -16.0$ mV, whereas the APTES-GA approach led to the lowest (most negative) value of $\zeta_i^* = -32.8$ mV. PPB-streptavidin lead to an intermediate value of $\zeta_i^* = -23.3$ mV. The baselines obtained for each of the functionalization approaches are shown in figure 4.3a.

The influence of the initial zeta potential, as obtained due to different functionalization strategies, on the overall detection signal of sEVs were further tested. The signals corresponding to each of the three functionalization approaches have been represented as bar plots in figure 4.3b. As a target, CD9

membrane proteins were captured using anti-CD9 antibodies. The concentration of the sEVs (3.5×10^8 particles/mL) as well as the duration of injection (2 hours) was kept the same in all cases. As seen, the signal ($|\Delta\zeta^*|$) was the highest in the case of PPB-avidin (16.3 mV) and lowest in the case of APTES-GA (3.9 mV). An intermediate signal was obtained in the case of PPB-streptavidin (7.4 mV). Hence, with reference to figure 4.3a, we observe that there is progressive signal enhancement as ζ_i^* becomes less negative. The response corresponding to the control measurements for each are also indicated as bar plots and are reasonably small.

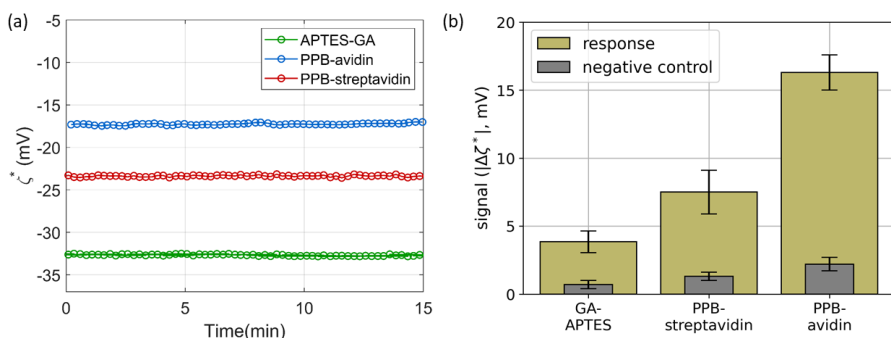


Figure 4.3 (a) Initial surface zeta potential, ζ_i^* of the sensor surface functionalized with PPB-avidin/streptavidin and APTES-GA. (b) The different values ζ_i^* are correlated with the different signals obtained with each of the functionalization approaches, when the CD9 surface protein on sEVs isolated from H1975 cells was targeted. PPB-avidin caused the strongest signal, while APTES-GA led to the lowest signal. Image adapted from Paper II [70] with permission from ACS Publications, licensed under CC BY 4.0.

4.3.4 Surface roughness

The signal depends not just on the charges but on structural factors such as the surface roughness as well, as explained in chapter 3. Here, we studied the level of surface roughness corresponding to the different functionalization approaches using an atomic force microscope (AFM). For this purpose, silica-based cover slips were used due to their resemblance with the capillary surface. The surface roughness corresponding to the APTES-GA and the PPB-avidin approaches were studied. Both the PPB surface as well as the PPB-avidin surface were studied separately in order to follow the evolution of the surface roughness at various stages of the PPB-avidin approach. The resulting AFM images are shown in figure 4.4. The scales of the images were adjusted for the optimal visibility. The values of the rms roughness (δ) were estimated for each of the surfaces. The APTES-GA surface had rather high δ at 1.5 nm.

The PPB surface had much lower δ at 0.7 nm while the PPB-avidin surface had a δ value of 0.8 nm.

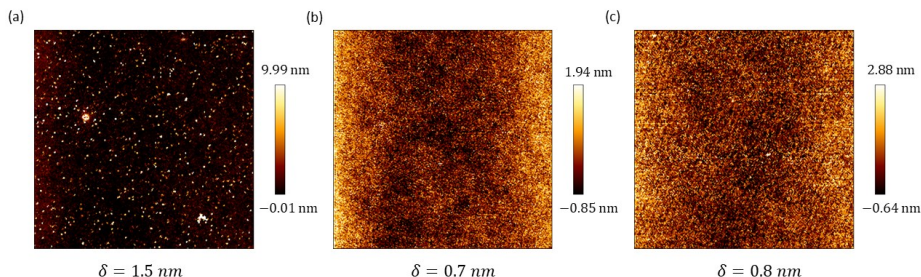


Figure 4.4 AFM images of silica-based cover slips functionalized with (a) APTES-GA (b) PPB and (c) PPB-avidin. The rms roughness, δ obtained for each image has been indicated below its panel. The images have been optimized for visibility. Image adapted from Paper II [70] with permission from ACS Publications, licensed under CC BY 4.0.

4.4.5 Simulations support the results

In order to understand the relationship between the charge contrast and the signal enhancement, we carried out simulations of the signal $\Delta\zeta^*$ as a function of the surface coverage, θ for different values of ζ_i^* . This was done following the model we adapted from the works of Adamczyk et. al., which we have discussed in chapters 2 and 3. The molecular zeta potential of sEVs (ζ_p) was assumed to have an average value of -30 mV for these simulations, following the results reported in literature [43], although this value can vary considerably for sEVs given their heterogeneity [44]. The results, as plotted in figure 4.5a, show that as the value of ζ_i^* increases from -30 to -10 mV, there is a progressive enhancement in the signal. This is because of the increasing charge contrast between the functionalized surface and the sEVs with the rise in ζ_i^* , resulting a stronger sensor response for the same extent of surface coverage. For a surface coverage of 5% for instance, the simulations show that changing the value of ζ_i^* from -30 to -20 mV, the signal is enhanced by a factor of 3, whereas increasing it from -20 to -10 mV leads to a further enhancement of about 1.5 times. A limitation of these simulations is the assumption that the surface is ideally smooth before the capture of the sEVs, while in reality, it does have some roughness to begin with, as shown by the AFM images.

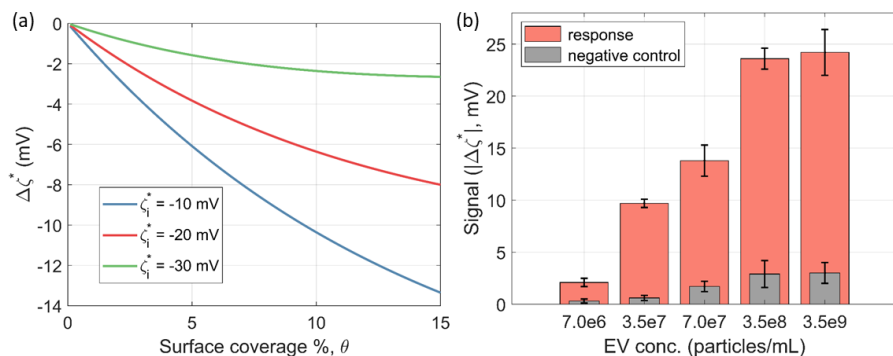


Figure 4.5: (a) The possibility to enhance the signal by modulating the values of ζ_i^* is shown using simulations. The dependence of the signal, $\Delta\zeta^*$ on θ was simulated for sEVs with $\zeta_p = -30$ mV, and $\zeta_i^* = -10, -20$ and -30 mV. (b) The dependence of the signal on the concentration of sEVs, when the CD9 membrane protein was targeted, following the PPB-avidin functionalization approach. Image adapted from Paper II [70] with permission from ACS Publications, licensed under CC BY 4.0.

4.5 Limit of detection

In order to further assess the improvement in the sensitivity in case of the PPB-avidin functionalization method, the limit of detection was estimated from a calibration curve, and compared with that in case of APTES-GA. sEVs derived from H1975 cells were used for this purpose, targeting the CD9 membrane protein. The concentration of the sEVs was varied from 7.0e6 to 3.5e9 particles/mL and the signal as well as the negative control was recorded. The results have been plotted in figure 4.5b. Each concentration of sEVs was injected for 2 hours. For determining the LOD, we define the minimum detectable signal (MDS) as $3 \times \text{SD}$ (standard deviation) of the baseline and estimated it to be 0.1 mV in our case. Then, we estimated the LOD to be 4.9×10^6 particles/mL. If we compare this with the LOD previously reported using the APTES-GA method [51], we note a 2 order of magnitude improvement with the PPB-avidin approach.

4.6 Examining a possible concern

So far, the results indicate that the PPB-avidin results in the highest signal among the three functionalization approaches studied here. This is also supported by the simulations. However, a key assumption we made in interpreting both the experimental results and the simulations is that there was no difference in the immobilized probe (antibody) density leading to a difference in the surface coverage, θ . It is important that we verify this assumption. For this

purpose, the surface coverages of sEVs captured by APTES-GA and PPB-avidin functionalizations were compared using a fluorescence microscopy technique, which allowed us to analyse the fluorescence signal from single sEVs. For this study, sEVs modified to express GFP-tagged CD9 were used. The fluorescence microscopy was performed using a Zeiss inverted microscope and a 100x oil immersion objective lens. It was further equipped with a Hamamatsu CCD camera (Orca Flash 4). The wavelength used for exciting the GFP proteins was 475 nm. The acquisition time was 2s and the images were recorded over an area of $133.2\ \mu\text{m} \times 133.2\ \mu\text{m}$ of a cover slip. Two such cover slips, one functionalized with GA-APTES approach and the other with PPB-avidin approach, were studied. The resulting images are shown in figure 4.6. The surface coverage of the sEVs captured by the APTES-GA method was on average about 10% higher than that captured by the PPB-avidin method. In the image shown in figure 4.6, a total of 567 sEVs were captured by APTES-GA, whereas in case of PPB-avidin, the number was 511. This suggests that despite capturing a lower number of sEVs, the PPB-avidin functionalization generates a higher net signal as compared to the APTES-GA method.

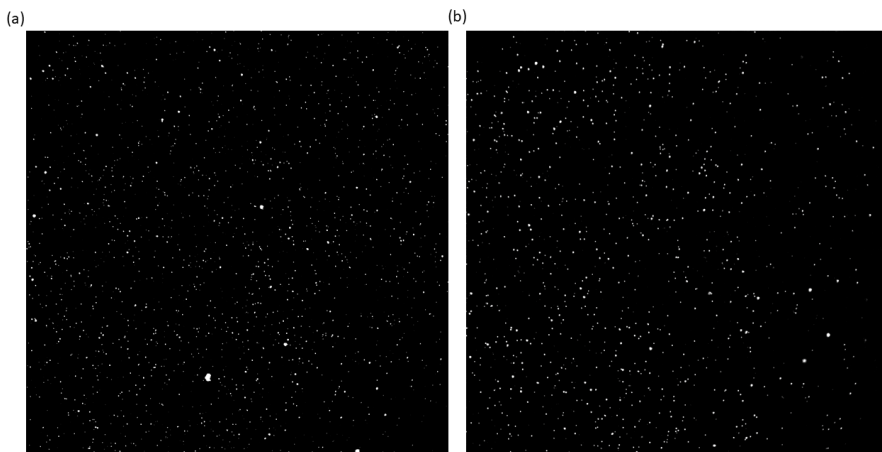


Figure 4.6: A comparison of the surface coverage of the sEVs captured using (a) APTES-GA and (b) PPB-avidin approaches. This was carried out optically using fluorescence microscopy. The sEVs were obtained from H1975 cells and expressed the GFP-CD9 protein. The average number of sEVs captured with the PPB-avidin approach was about 10% less. Image adapted from Paper II [70] with permission from ACS Publications, licensed under CC BY 4.0.

4.7 Applications

Having demonstrated a clear enhancement in sensitivity with surface charge optimization, we then explored some applications of the method. The method

was first applied in a model system, consisting of NSCLC cell line, to study the prospect of monitoring the treatment response of targeted cancer medicine by analysing the membrane protein expression levels of EVs which were collected from cells under different treatment regimens. In addition, the method was applied to clinical sEVs collected from the pleural effusion of adenocarcinoma patients. Table 4.1 gives the details of the samples used for this study.

Table 4.1: Details of the sEVs isolated from the H1975 cells and the pleural effusion fluid for validating the improved surface functionalization approach used for profiling the membrane proteins of the sEVs. Table adapted from Paper II [70] with permission from ACS Publications, licensed under CC BY 4.0.

sample	treatment	tumor stage	genomic alteration	feature
H1975 cell line	untreated	--	EGFR exon 21, L858R, exon 20 T790M	
	erlotinib	--		resistant
	osimertinib	--		responsive
PE 002	ALK-TKI crizotinib	T2aN0M1a	EML4-ALK variant 3 (a/b)	responsive
PE 011	EGFR-TKI erlotinib	T4N2M1a	EGFR exon 21, L858R	progressive

4.7.1 Treatment monitoring

Cells treated with targeted cancer medicines would respond in terms of the membrane protein expression levels of the sEVs originating from them. To investigate this, we used sEVs derived from the cell culture media of EGFR-mutant NSCLC cells before and after they were treated with two kinds of EGFR-TKI treatments: erlotinib and osimertinib. These are standard treatments that are clinically used for those NSCLC patients where EGFR mutation is the driving factor [74]. Furthermore, studies indicate that the protein PD-L1 is expressed when the tumor is driven by EGFR [74]–[76] and it plays a vital role in bypassing the immune system response [77]. Hence, we investigated the PD-L1 and EGFR protein profiles in our study of the sEVs prior and post EGFR-TKI treatments. The dose of the treatment chosen was 1 μ M of erlotinib and 0.1 μ M of osimertinib for 48 hours. Figure 4.7a shows the expression levels of CD9, EGFR and PD-L1 of the sEVs along with the corresponding negative controls. The concentration of the sEVs for profiling the CD9 and EGFR expression levels was 3.5e7 particles/mL, while in case of PD-L1, the concentration was chosen to be 10-fold higher, as the signal was otherwise too small (data not shown). From the data, we observed that the expression level

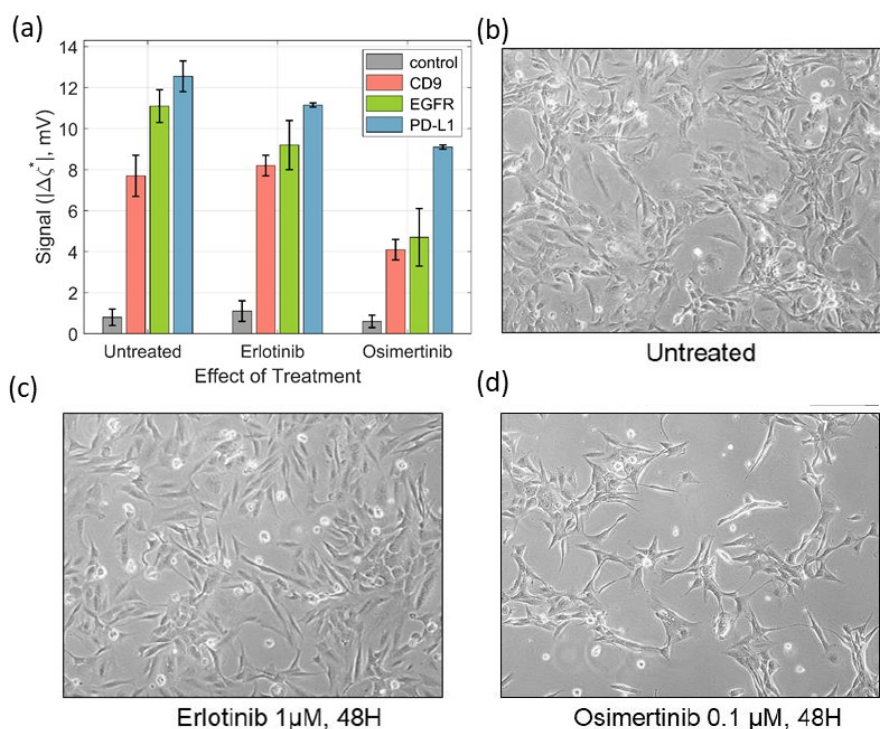


Figure 4.7 (a) Influence of the cancer treatments on the surface protein (CD9, EGFR, PD-L1) profiles of the sEVs isolated from H1975 cells. These cells were subject to EGFR-TKI treatments: erlotinib and osimertinib. The measurements show relatively modest effect of the erlotinib treatment on the protein expression levels, whereas the osimertinib treatment show a stronger decline in the expression levels of all the three proteins. The morphology of the H1975 cells that were (b) untreated, and treated with (c) erlotinib and (d) osimertinib. The treated cells were then harvested from the cell culture media and analysed using a Nikon Eclips TS100 microscope using a 10x lens. The images were then processed using Adobe Photoshop. Image adapted from Paper II [70] with permission from ACS Publications, licensed under CC BY 4.0.

of CD9 remains rather unchanged before and after treatment with erlotinib. Further, the levels of EGFR and PD-L1 were reduced by 20% and 10% respectively. On the other hand, the effect of osimertinib treatment was much stronger. In comparison to the sEVs from the untreated cells, the osimertinib cells produced sEVs that had CD9, EGFR and PD-L1 levels decreased by 50, 60 and 30% respectively. A study of the cell morphology was also done using a Nikon Eclips microscope. A 10x lens was used and the images are shown in figure 4.7 b-d before and after the treatments with erlotinib or osimertinib. The erlotinib treatment did not significantly affect the cell viability. The osimertinib treatment on the other hand significantly affected the viability of the cells after 48 hours. The cell viability was reduced by about 50% at the end of 72

hours (data not shown). The relatively modest response of the cells to erlotinib in this case also lines up with other studies reported in literature [78].

4.7.1 Liquid biopsy with reduced sample volume

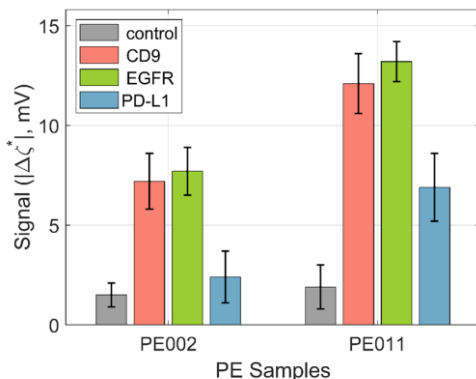


Figure 4.8: Liquid biopsy with reduced sample volume done with the PPB-avidin approach. The surface protein CD9, EGFR and PD-L1 were profiled on sEVs derived from the PE fluid of NSCLC patients PE002 and PE011. The trends in the expression levels could be profiled with 100 times less volume in case of CD9 and EGFR, and 10 times less volume in case of PD-L1, compared to previously reported values with the APTES-GA approach. Image adapted from Paper II [70] with permission from ACS Publications, licensed under CC BY 4.0.

A higher detection sensitivity means that the required sample volume for analysis can be significantly reduced. This prospect is particularly advantageous for clinical sample which are very precious. To demonstrate this prospect, we analysed sEVs derived from the pleural effusion (PE) fluid of two NSCLC adenocarcinoma patients, labelled as PE002 and PE011. These patients suffered from tumors driven by ALK-fusion and EGFR mutation respectively. Further details can be found in table 4.1. Three surface proteins, i.e. CD9, EGFR and PD-L1 on these sEVs were profiled using the PPB-avidin functionalization method. The results are plotted in figure 4.8 along with the negative control. The qualitative trends of the surface-protein profiles match with those reported earlier using the streaming current method [69], as well those reported using immuno-PCR and western blot analyses [48]. However, the results using the present method were obtained using 100 times less sample volume in case of CD9 and EGFR proteins, and 10 times less volume in case of the PD-L1 proteins, compared to that reported earlier with the APTES-GA approach.

4.8 Surface charge density

The key parameter that we intended to modulate using the different surface functionalization strategies here was the surface charge density, σ . It is therefore important to estimate σ in order to draw a clear physical picture of the surface-level changes taking place in the sensor. We start from the relation that expresses the surface charge density of a flat surface in contact with an electrolyte. This was obtained by solving the Poisson-Boltzmann equation under ideal conditions. Normally, Poisson-Boltzmann equation is challenging to solve analytically, and is instead done numerically. However, in the one-dimensional case, an exact non-linear solution can be obtained analytically. This is known as the Gouy-Chapman equation [79] and is given by:

$$\sigma = [8cN\epsilon_r\epsilon_0k_BT]^{1/2} \sinh\left(\frac{e\psi_0}{2k_BT}\right) \quad \dots(4.1)$$

where c is the ion concentration, $\epsilon_r\epsilon_0$ refers to the permittivity of the medium, N is Avogadro's number, T is the temperature and ψ_0 is the surface electrostatic potential. This solution is however valid for an ideally flat surface. From the AFM images shown in figure 4.4, we saw that the surface does have a roughness, although small. In this situation, equation 4.1 provides a lower bound to the value of σ [79]. We define the term effective charge density, σ_{eff} as the sum of the charge density of the flat surface as well as the surrounding ions within the slip plane [79]. In that case, the surface electrostatic potential, ψ_0 will get replaced by the surface zeta potential, ζ_i^* . This results in the equation,

$$\sigma_{eff} = [8cN\epsilon_r\epsilon_0k_BT]^{1/2} \sinh\left(\frac{e\zeta_i^*}{2k_BT}\right) \quad \dots(4.2)$$

Using equation 4.2, the σ_{eff} of various functionalization approaches were estimated, and are given in the table 4.2. The values of ζ_i^* were obtained from the measurements. The σ_{eff} of a clean capillary surface was estimated to be $-5.2 \times 10^{-3} \text{ e/nm}^2$. The APTES-GA coating only partially screen the negative charges and the surface retains a strong negative charge density, $-2.0 \times 10^{-3} \text{ e/nm}^2$. As both PLL and avidin are positively charged, functionalization with PPB-avidin led to the least negatively charged surface, with a σ_{eff} value of $-0.8 \times 10^{-3} \text{ e/nm}^2$. The sEVs on the other hand are strongly negatively charged at physiological pH due to the presence of deprotonated COO^- group of proteins, acidic sugars and/or exposed phosphates of DNA [43].

Hence, the PPB-avidin leads to the largest charge contrast among the approaches tested.

Table 4.2: Measured values of ζ_i^* and estimated values of σ_{eff} for the sensor surface at various stages of functionalization. PPB-avidin produced the least negative charge density among the others. Table adapted from Paper II [70] with permission from ACS Publications, licensed under CC BY 4.0.

surface	ζ_i^* (mV)	$\sigma_{eff}(10^{-3} \text{e/nm}^2)$
bare silica	−68.6	−5.2
GA-APTES	−32.5	−2.0
GA-APTES-anti-CD9	−32.8	−2.0
PPB	−26.3	−1.6
PPB-avidin	−14.1	−0.8
PPB-avidin-anti-CD9	−16.0	−0.9
PPB-streptavidin	−20.7	−1.2
PPB-streptavidin-anti-CD9	−23.3	−1.4

4.9 Chapter summary

This chapter extended the discussion on the electrostatic charge contrast introduced in the previous chapter, and examined it experimentally by modulating the charge density on the sensor surface. Testing three different functionalization strategies showed a clear correlation between the charge contrast and the signal generated by the capture of sEVs. The optimized functionalization strategy with PPB-avidin led to an improvement in the LOD by two orders of magnitude. This was then utilized to demonstrate highly sensitive profiling of membrane proteins of sEV both from clinical samples collected from NSCLC adenocarcinoma patients and a cell-line-based model system designed to examine the prospect of treatment monitoring of targeted cancer medicines. Other than improved sensitivity, the new approach with optimized charge contrast also allowed analysis from a lower sample volume than was shown earlier using the same method.

5. Electrokinetic Sandwich Assay

5.1 Improving sensing selectivity

Having explored some of the critical parameters that the signal of our sensor depends on, we now turn our attention to another aspect vital in biosensing: selectivity. In case of immunoassays in particular, the detection of a target often suffers from low selectivity due to numerous non-specific reactions and cross-reactivity [21], [80], [81] of the affinity probes with non-target molecules. This can be especially problematic when the target is to be detected from a complex medium such as plasma or serum. Sandwich immunoassay is a well-established, and widely used method to overcome this challenge [82]–[84]. This method involves detecting the target with two affinity probes, a capture probe and a detection probe, which are directed to different epitopes of the same target. The target is first captured with the capture probe, and then “sandwiched” by the detection probe, which binds to a different binding site. This approach leads to a considerable reduction in the non-specificity and cross reactivity. Sandwich assays are however usually accompanied by the use of labels for generation, or even amplification of the signal [81]. Examples of such labels are enzymes [85], nano-particles [86] and fluorescence tags [87] conjugated to the detection antibodies. However, label-free approaches to sandwich assays, in electrical sensors particularly, have been lacking. In this chapter, we demonstrate the proof of principle of an electrokinetic sandwich assay, realized using the streaming current method for specific detection of biomolecules. The detection was carried out both in the PBS buffer, as well as a complex medium (*E. coli* cell lysate) with a higher specificity as compared to the direct assay.

5.2 Direct assay vs. sandwich assay and the model system

The schematic illustrations of direct and sandwich assays are shown in figure 5.1. A direct assay consists of a single type of probe, called capture probe, to which the target binds. A sandwich assay on the other hand has two kinds of probes. A capture probe captures the target, and then a detection probe binds to a different binding site on the captured target, thereby inducing a signal. In

this study, we used the immunoglobulin-binding Z-domain and the therapeutic monoclonal antibody trastuzumab (IgG) as the model affinity pair. The Z-domain was derived from the B domain of the staphylococcal protein A. The trastuzumab was used as the target molecule while the Z-domain was used both as the capture, as well as the detection probe, targeting two different binding sites in the Fc region of the trastuzumab [88]. The choice of this pair was motivated by the simplicity of using the same molecule as both the capture and detection probe. An additional advantage was the fact that the pair also has a reasonably good charge contrast, which is required for a sensitive detection, as discussed in chapter 3. At the measurement pH of 7.4, Z-domain had a net negative charge ($\zeta_p = -7.1 \pm 0.8$ mV), while trastuzumab was positively charged ($\zeta_p = 21.4 \pm 0.3$ mV). This pair was thus used to demonstrate a label-free electrokinetic sandwich assay. Further, the zeta potential of the detection probes was modulated by conjugating single-stranded DNA oligonucleotides, letting us achieve a higher detection sensitivity. Measurements performed with varying lengths of the conjugated DNA showed that the sensitivity increases with the length of the DNA.

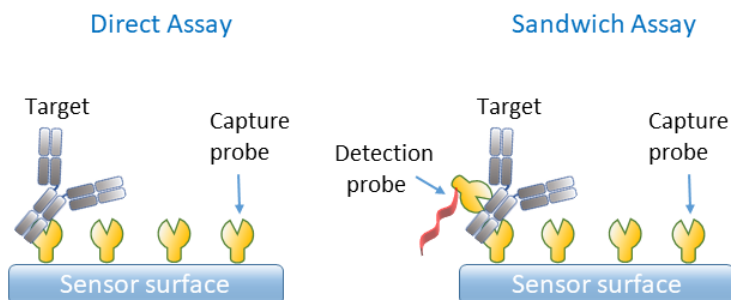


Figure 5.1. Schematic illustrations comparing direct and sandwich assays. A direct assay has a single capture probe to which the target binds, whereas a sandwich assay has a capture and a detection probe that bind to different binding sites of the same target. Image adapted with permission from Paper III [60]. © 2020 Elsevier B.V.

5.3 Proof of principle of an electrokinetic sandwich assay

In order to demonstrate the proof of principle of an electrokinetic sandwich assay, we used silica micro-capillaries. The fluidic connections and electrical measurements were similar to the ones described in chapter 3. The surface functionalization was also identical to that described in chapter 3 until the preparation of the GA surface. Thereafter, 5 μ M of the Z-domain was immobilized on the GA surface for 1 hour. This was followed by deactivating the unreacted aldehyde groups with Tris-ethanolamine (0.1 M Tris buffer and 50

mM ethanolamine, pH 0.9) for 30 minutes. Non-specific interactions were further reduced by treating the functionalized surface as well as the inner surfaces of the connecting tubes and hollow electrodes with 0.05% w/v casein solution for 30 minutes. The capillaries were then stored under nitrogen atmosphere at 4°C until the measurement. A schematic of the complete measurement sequence is shown in figure 5.2a. The baseline measurements were done as described in chapter 3. The target was injected after the first baseline, at a constant pressure of 1.5 bar. The rate of the target conjugation could be tracked by monitoring I_s . The target injection was carried out until an equilibrium in the value of I_s was achieved. This was followed by measurement of the 2nd baseline. As the target-probe interaction is a dynamic one, switching from the sample injection to the PBS buffer drove the reaction in the reverse direction, causing dissociation of the target-probe pair. Therefore, the duration of the second baseline was fixed at 20 minutes. The detection probe was then injected at a concentration of 200 nM. This was followed by the recording of the third baseline. During this phase, there were two overlapping processes: the dissociation of the target from the capture probe, and the dissociation of the detection probe from the target. Hence, for estimating the signal, a fixed point at 20 minutes past the beginning of the third baseline was considered. There are two signals associated with this type of measurement. The first one is the signal from the direct assay step due to binding of the target to the capture probe and is defined as the difference between the end point of the second baseline and the average value of the first baseline, $\Delta\zeta_D^* = \zeta_2^* - \zeta_1^*$. The second is the signal from the sandwich assay step, due to the binding of the detection probe with the target, and is defined as the difference between the end points of the third and second baselines, $\Delta\zeta_S^* = \zeta_3^* - \zeta_2^*$.

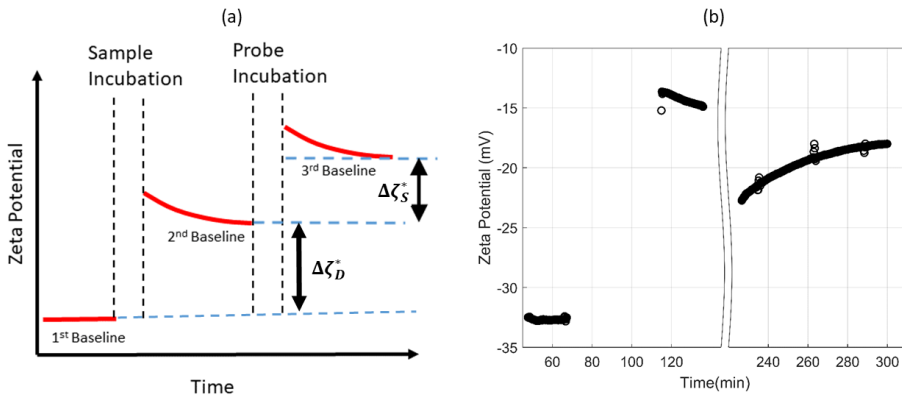


Figure 5.2. (a) The multi-step measurement sequence for the sandwich assay. The measurement of the first baseline is followed by the injection of the target until equilibrium is reached. The second baseline is then recorded for 20 minutes. This is followed by the injection of the detection probe. Finally, the third baseline is measured. (b) Exemplary experimental data corresponding to this measurement sequence. Image adapted with permission from Paper III [60]. © 2020 Elsevier B.V.

Exemplary data corresponding to the multi-step measurement sequence is shown in figure 5.2b. The initial baseline corresponding to the immobilized Z-domain capture probes had an apparent zeta potential (ζ_1^*) of -32.5 ± 0.3 mV. Upon binding with the positively charged trastuzumab (T) molecules at 100 nM concentration, the baseline became less negative (shifted upwards). The end point of the second baseline (ζ_2^*) value of -15.1 ± 0.8 mV. In the final step, due to the binding of the negatively charged Z-domain detection probes, the baseline (ζ_3^*) became more negative (shifted downwards). The signals corresponding to the direct assay and sandwich assay steps are shown as bar plots in figure 5.3a and 5.3b respectively. These signals were recorded for T concentrations of 200 pM, 1 nM, 10 nM, 100 nM and 1 μ M. From the bar plots, we observed the following for the entire concentration range of T: the magnitude of the signal increases with the T concentration for both direct and sandwich assay, the magnitude of the signal in case of the direct assay was higher than that of the sandwich assay step and the sign of the signal in case of the direct assay was positive whereas the sign of the signal in case of the sandwich assay step was negative. The results indicate that the direct assay has better limit of detection in comparison to the sandwich assay step. The injection of 1 nM of T for instance led to 8.9 ± 0.9 mV of signal in case of the direct assay, but only -1.2 ± 0.2 mV in case of the sandwich assay

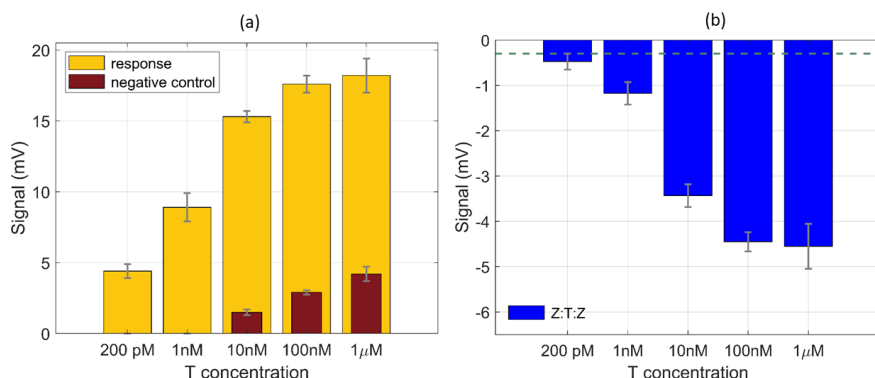


Figure 5.3. Comparison of the signal from the (a) direct assay and (b) the sandwich assay for various concentrations of T. The signal from the direct assay is considerably higher in magnitude than the sandwich assay, and they have the opposite sign. The negative controls in case of the direct assay are shown as bar plots, whereas for the sandwich assay, they are shown as a dotted line. Image adapted with permission from Paper III [60]. © 2020 Elsevier B.V.

step. However, rather than comparing the magnitude of the signals directly, we also must consider the extent of non-specific interaction. Hence, we also carried out negative control in both cases, and they are represented as bar plots in figure 5.3a and as a dotted line in figure 5.3b. The negative control in case of the direct assay involved injection of the target in an identically prepared

capillary, but without the capture probes. On the other hand, the negative control in case of the sandwich assay involved measuring the extent of interaction of the detection probe with the immobilized capture probes without any captured target. Clearly, the negative control in case of the sandwich assay produced a much weaker response as compared to the direct assay. The response from the negative control in case of the direct assay corresponding to 100 nM of T was found to be 1.5 mV, which was about 17% of the signal. In case of the sandwich assay, it was 7.3% of the signal for the same concentration of T. Thus we observed that the lower overall signal in case of the sandwich assay is partially compensated by a lower extent of non-specific interaction.

5.4 Signal enhancement by DNA conjugation

In chapter 3, we had shown how the size and charge of the target influences the signal. In particular, we had shown that when the surface and the binding protein has the opposite type of charge i.e. a larger charge contrast, the sensitivity is higher. In the present case, this implies that if the sensor surface becomes less negative upon the target capture, we can enhance the signal from the sandwich assay step by making the detection probe more negative. Such a charge dependence has been reported in literature [36], [38], [54], but it has not been studied for immunoassays. To modulate the ζ_p of the detection probes, we conjugated them with single stranded DNA that was 15 nucleotides long. The resulting detection probe (Z – DNA₁₅) was more negative ($\zeta_p = -9.3 \pm 0.8$ mV) than the Z-domain ($\zeta_p = -7.3 \pm 0.8$ mV). The ζ_p of the probes were measured by electrokinetic light scattering (ELS) and the values are given in table 5.1. The responses of the sensor against the binding of the Z – DNA₁₅ detection probes for various concentrations of T are given in figure 5.4a. A clear signal enhancement was seen for the entire concentration range in this case when compared to using Z as the detection probe. The limits of detection were estimated to be ~ 140 pM in case of Z and ~ 90 pM in case of Z – DNA₁₅.

To further investigate the effect of DNA-conjugation with the detection probes, we used DNA oligonucleotides of different lengths conjugated to Z-domain. Their details are given in table 5.1. The sensor responses corresponding to the sandwich assay step when 100 nM of T is used as the target, and Z, Z – DNA₅, Z – DNA₁₅ and Z – DNA₃₀ were used as detection probes are shown as bar plots in figure 5.4b. As the length of the DNA increased from 5 to 30 nucleotides, it can be seen that the signal from the sandwich assay also increased proportionately. The signal corresponding to Z – DNA₃₀ was about 300% higher than that for Z – DNA₅ for the same concentration of T. This further validates the claim made in chapter 3 about the influence of molecular

charge in determining the signal. We further scrutinized these results by a theoretical analysis, as presented in section 5.5. A clear departure from this trend however was seen when we compared the signals corresponding to Z with that of Z – DNA₅. Despite carrying a stronger negative charge, the signal obtained with the latter was in fact lower in comparison to that of the former.

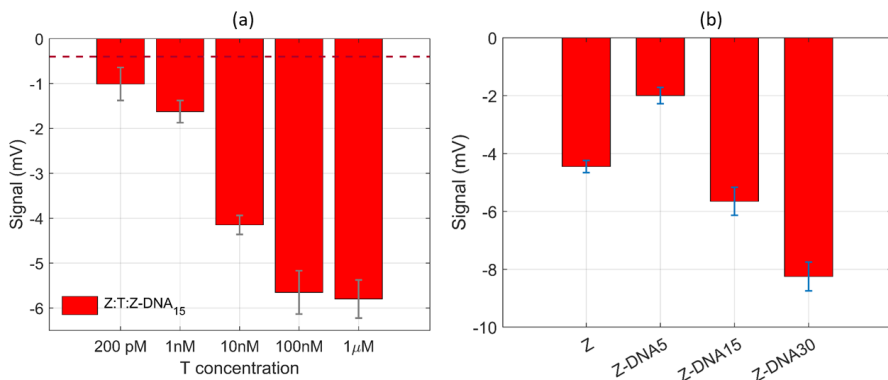


Figure 5.4. Signal enhancement with DNA-conjugation with the detection probes. (a) Signal for various concentrations of T when Z – DNA₁₅ is used as the detection probe. (b) Signal for various lengths of DNA conjugated to Z for a fixed concentration of T. Image adapted with permission from Paper III [60]. © 2020 Elsevier B.V.

5.5 Simulations

In the previous chapter, we used the Adamczyk model [34] to explain the influence of size and charge of a target on the signal. Here, we utilize the same model to check if it can explain the difference in the signals obtained for the direct and the sandwich assay, as well as the effect of conjugation of DNA of various lengths to the detection probes. Using equation 3.3, the signals $\Delta\zeta^*$ for the various detection probes were plotted as a function of the surface zeta potential of the surface ζ_i^* and the molecular zeta potential, ζ_p of the target molecules. In case of the direct assay, $\zeta_i^* = \zeta_1^*$, that was measured to be -32.5 mV, and the value of ζ_p corresponded to that of the T molecules. On the other hand, for the sandwich assay step, $\zeta_i^* = \zeta_2^*$ that was measured to be -15.0 mV after immobilization of 100 nM of T, and ζ_p in this case corresponded to the molecular zeta potential of detection probe use. The ζ_p values of T and the unconjugated as well as the DNA-conjugated detection probes were measured by ELS (see section 2.6 for details) are given in table 5.1. The simulated plots as a function of the surface coverage for both direct assay (Z – T) and sandwich assay (Z – T – Z – DNA_x, where $x = 5, 15, \text{ or } 30$) are shown in figure 5.5. The simulations predict a strong and positive signal for the direct assay (blue curve), and a considerably weaker, negative signals for

the sandwich assays (remaining curves). Moreover, as the ζ_p of the detection probes become more negative upon conjugation of DNA of various lengths, the simulations predict a consistent enhancement of the signal. Upon comparison with the experimental results presented in figures 5.3 and 5.4, we see a very good agreement with the simulations in general. A notable exception to this trend is the fact that Z – DNA₅ induces a smaller signal as compared to Z, despite carrying a stronger negative charge (figure 5.4b). In addition to the charge, the size of the molecules is also expected to play a role, as discussed in the chapter 3. The stronger signal of the direct assay in comparison to that from the sandwich assay is also partly due to their size difference. The hydrodynamic radii of Z and T are 0.6 and 1.5 nm respectively. As a result, T is able to offer a stronger impedance to the flow of ions in the electrical double layer as compared to Z, leading to a stronger net signal.

Table 5.1: Details of the probes and the target. Their ζ_p values were measured by electrophoretic light scattering (ELS). Table adapted with permission from Paper III. © 2020 Elsevier B.V.

Symbol	Protein	Conjugation	ζ_p (mV)
T	Trastuzumab	–	21.4 ± 0.3
Z	Z-domain	–	-7.1 ± 0.8
Z – DNA₅	Z-domain	5 nt DNA	-9.3 ± 0.8
Z – DNA₁₅	Z-domain	15 nt DNA	-12.9 ± 0.5
Z – DNA₃₀	Z-domain	30 nt DNA	-20.1 ± 0.9

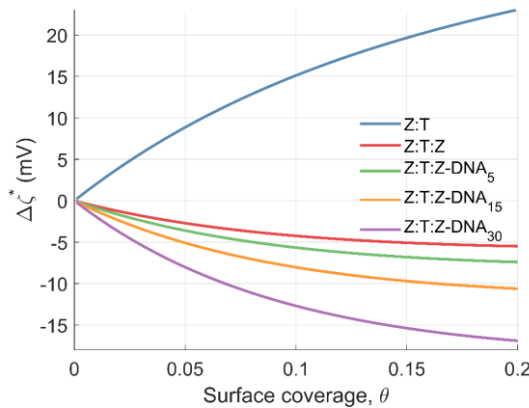


Figure 5.5. Simulations comparing the signal from the direct and sandwich assays. The signal generated from the sandwich assay is considerably weaker in comparison to that of the direct assay and has negative sign. Moreover, the simulations predict the possibility to enhance the signal by making the ζ_p of the detection probes more negative via DNA-conjugation. Image adapted with permission from Paper III [60]. © 2020 Elsevier B.V.

5.6 DNA-conjugation and affinity

The fact that the signal from Z – DNA₅ is lower in comparison to Z in the sandwich assay step defies not only the general trend of the increasing signal with the ζ_p of the detection probes (figure 5.4b), but also deviates from the

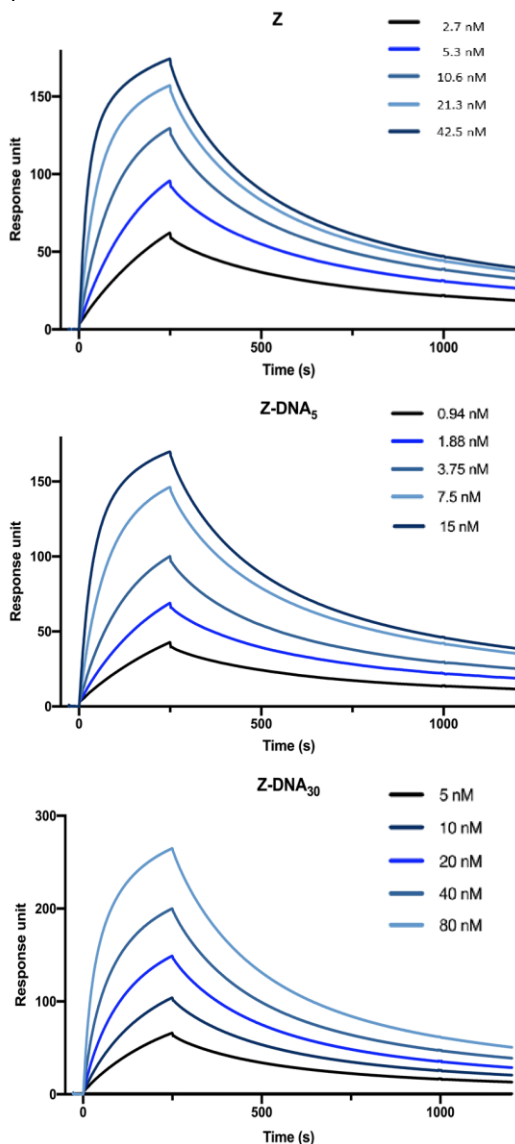


Figure 5.6: SPR sensorgrams corresponding to the interaction between T and Z, Z – DNA₅ and Z – DNA₃₀ respectively for various concentrations of T. The K_D values extracted from these show a small decrease in the affinity upon DNA-conjugation with Z-domain, with the decrease being higher with the length of the conjugated DNA. Image adapted with permission from Paper III [60]. © 2020 Elsevier B.V.

simulations corresponding to these two probes. We speculated that this may be caused by a reduction in affinity between the Z-domain and T as a result of DNA oligonucleotides. To investigate if this was indeed the case, we performed SPR measurements (using a Biacore 8K system) of the affinity constants of the detection probes towards T. This was carried out by immobilizing T as a ligand on a CM5 chip surface and then flowing Z, Z – DNA₅ and Z – DNA₃₀ over it separately. Figure 5.6 shows a representative sensorgram depicting the interaction between T with each of the probes, for various concentrations of T. The values of the equilibrium dissociation constant (K_D) were calculated to be 0.89, 1.12 and 3.76 in case of Z, Z – DNA₅ and Z – DNA₃₀ respectively. There was hence a small increase in K_D , i.e. a small decrease in the interaction affinity between T and the Z – DNA_x as a result of the DNA-conjugation to Z. Moreover, this reduction in affinity scaled with the length of the conjugated DNA oligonucleotides. This leads us to an important result. The higher sensitivity with the DNA conjugated probe comes despite a slight decrease in the affinity. This implies that the influence of charge on the signal more than compensates the loss due to a decrease in the affinity. The data shown in figure 5.4b suggests that this compensation is not sufficient in case of Z – DNA₅, which could explain why its signal is less than that of Z alone, when used as a detection probe. In principle, one could repeat these measurements with much higher lengths of the DNA conjugated to the probes in order to enhance the signal further, to perhaps exceeding the signal from the direct assay. Of course, there may be a point at which the decrease in affinity would be large enough to eliminate additional the signal enhancement. This could be an interesting aspect to investigate in a future study.

5.7 Application: detection of target from a complex medium

A key motivation for studying sandwich assays is that they offer better specificity as compared to the direct assay. In order to demonstrate this aspect, we carried out detection of Trastuzumab from a complex medium. We chose the *E. coli* cell lysate as the medium, since the bacterial lysate offers a plethora of various proteins [89]. Apart from being a suitable choice for putting the claims about specificity to test, it also prevents the formation of aggregates [89]. Although aggregation can sometimes be exploited for detection with superior sensitivity [90], its effect on the signal generated in our case would hamper the theoretical analysis. For use as a complex detection medium, the lysate was diluted 100 times with 1 × PBS, primarily to reduce its viscosity. This was followed by spiking T to it, and adjusting the final concentration of T to 100 nM. The signal corresponding to the direct and sandwich assays were then

recorded, along with the negative controls. Z – DNA₃₀ was used as the detection probe. These results have been plotted as bar plots in figure 5.7. The resulting signal corresponding to the direct assay was 18.7 ± 0.9 mV while that for the sandwich assay was -4.3 ± 0.3 mV. Three kinds of negative controls were performed for the sandwich assay step in order to test the various possible types of non-specific binding. The control C₁ involved excluding the immobilization of the capture probes from the surface functionalization, and then injecting only the lysate medium without the target. This produced a signal of 2.3 mV. The control denoted as C₁ + T was similar to C₁, but involved injecting 100 nM of T spiked to the lysate. This generated a signal of 3.6 mV. Finally, the control C₂ involved injecting the unspiked lysate over the Z immobilized surface. This produced a signal of 2.7 mV. The negative control corresponding to the sandwich assay step, denoted as C₂ + Z – DNA₃₀ involved the same steps as C₂, followed by the injection of Z – DNA₃₀. This led to the smallest response among all the controls, -0.3 mV. For better comparison of these values, we define the term specificity ratio (SR) as the ratio of the signal corresponding to the target / detection probe injection to that generated by its corresponding negative control. In case of the direct assay step, the values of SR for C₁, C₁ + T and C₂ were 5.2, 8.1 and 6.9 respectively. SR in case of the sandwich assay (C₂ + Z – DNA₃₀) on the other hand was 14.3. The sandwich assay hence showed a considerably higher SR in case of the direct assay.

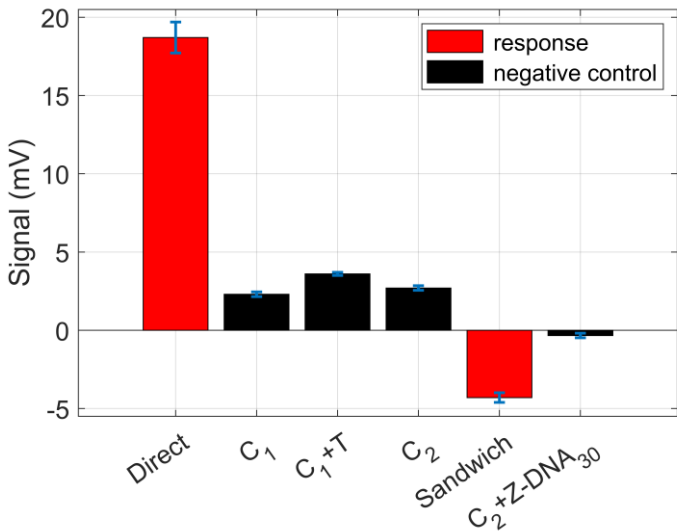


Figure 5.7: Signals from the direct and sandwich assay detection of T from an *E. coli* cell lysate medium, along with various negative controls corresponding to each. The specificity ratio (SR) is much higher in case of the sandwich assay as compared to the direct assay. Image adapted with permission from Paper III [60]. © 2020 Elsevier B.V.

5.8 Chapter Summary

In this chapter, we addressed a key area of biosensing: specificity. We showed how the specificity could be improved in this sensing method, by demonstrating a proof of principle of an electrokinetic sandwich assay. While the sandwich assay in our case showed a weaker signal and had an extra step in the detection in comparison to the direct assay, we showed a clear benefit by improving the specificity of detection. Moreover, we demonstrated that the weaker signal could be overcome by conjugating DNA oligonucleotides with the detection probes. Such a conjugation alters the zeta potential of the probes, and thereby the charge contrast with the target. All these observations were supported by simulations carried out using an established theoretical framework. We also showed an application by carrying out target detection from a complex medium consisting of *E. coli* cell lysate, and demonstrated a clear improvement in specificity in case of the sandwich assay.

6. Multiplexed membrane protein profiling of extracellular vesicles using charge-labelled antibodies

The lipid membrane of sEVs have numerous surface proteins [45], [51]. The presence and relative abundances of these membrane-bound proteins vary widely depending on the cellular source of EVs, their route of biogenesis and also the activation status of the parental cell [46]. As a result, the membrane protein composition of EVs are extremely heterogeneous even when they are collected from a single cellular source. Such a heterogeneity means that an average analysis on the entire EV population is less effective to reveal its biomarker potential. Instead, analysis on a sub-population level, e.g. defined by the presence and/or differential expression levels of a set of membrane proteins, is more likely to provide important biological/pathological information. It is therefore essential to develop methods that can assess the differential expression of multiple membrane proteins on a subset and the relative abundance of various subpopulation in a given biological sample. Fluorescence labelling of the membrane proteins and various single EV assays have been recently been developed to address these issues [44], unlocking enormous diagnostic and therapeutic opportunities. Thanks to these developments, a clear need has emerged for a diagnostic tool that can quickly analyse a specific subset of sEVs and accurately determine the differential expression of multiple membrane proteins. A microchip-based method that can perform such analyses with a small amount of sample will clearly have great advantages over the existing fluorescence-based techniques, potentially accelerating the implementation of sEV-based diagnosis in practice.

In this chapter we describe the development of such a microchip-based method to analyse the differential expression level of multiple membrane proteins of sEVs. The method is a culmination of the developments described in the previous chapters and extension of two key technologies. First, we implemented the streaming current-based sensor on a microchip, which were fabricated on Si substrates and secondly, we developed electrostatic labelling strategy to label antibodies with either positive or negative charges. The latter allows performing more accurate profiling of surface proteins and stepwise measurement of multiple surface proteins on the same sEV population, which

can be captured either with an antibody or non-specifically. This would provide the option to probe either a particular sEV sub-population defined by a membrane protein, or the entire sEV population in the sample.

6.1 Micro-chip based sensing

The microchips used for the sensing were fabricated using silicon-glass microfluidic technology where the channels were fabricated on silicon substrate and sealed by bonding with glass wafer. The details about the fabrication are described in Paper V [91]. Briefly, rectangular channels ($10 \times 25 \mu\text{m}$) were etched on Si substrates using reactive ion etching. Subsequently, it underwent anodic bonding to a thin quartz glass for sealing. A schematic of the procedure is shown in figure 6.1a-c. In order to allow interfacing with the standard microfluidic connections, a custom-built chip manifold was also designed from PEEK material. It was tested to be leak-free upto 6 bar of pressure. An image of the manifold is shown in figure 6.1d. The microchip outperformed the capillary in terms of sensitivity, mainly due to the high surface quality of the thermally grown silicon oxide [91].

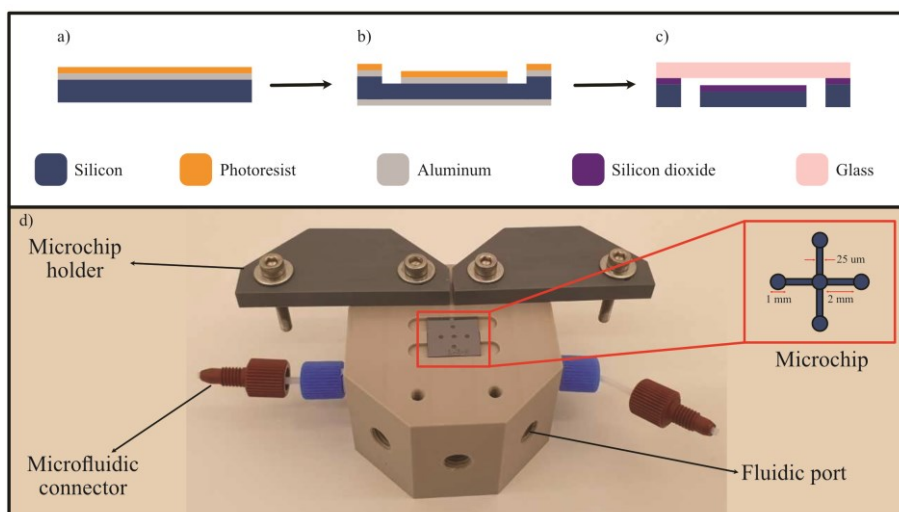


Figure 6.1. (a-c) A schematic of the various steps involved in etching the channels in the silicon/silicon dioxide wafer, followed by sealing with glass by anodic bonding. (d) An image of the manifold used for interfacing the chip with the standard microfluidic connectors.

6.2 A labelling strategy for multi-marker membrane profiling

The prospect of analysing membrane protein expression level by using streaming current measurement has been shown by us using a direct assay approach [51], where we also demonstrated that the method can detect a difference in the expression level. This type of direct assay for the membrane protein analysis has two limitations. First, the expression level of a membrane protein is estimated from the surface coverage of the bound sEVs. Since the sEVs having a higher expression level of a target protein are more likely to bind to the surface-immobilized antibodies, the sensor response does depend on the expression level. However, this is an indirect way to analyse the expression level of transmembrane proteins. The second limitation is that the multi-markers analysis, which should ideally be done on a single population, is performed by capturing different population in different channels by immobilizing different antibodies [69]. Both of these limitations hinder the prospects and accuracy of sEV-based diagnosis. A practical way to overcome these challenges would be to capture a single population on the sensor surface and analyse different membrane proteins, e.g. a labelling strategy similar to one normally done in fluorescence-based methods. The labels must induce a detectable signal in the streaming current technique. Such a labelling strategy can be designed by exploiting the charge influence on the sensor response as described in the preceding chapters.

6.3 Electrostatic labels and proof of concept study

As shown in chapter 3 and 5, the ζ_p of the detection probe plays a pivotal role in signal amplification. In chapter 5, we demonstrated that by conjugating DNA oligonucleotides, the value of ζ_p of an antibody can be tuned to achieve negatively charged probes. In a similar manner, the ζ_p of an antibody can also be modulated to achieve positively charged detection probes, e.g., by conjugating L-lysine based polymer units. Before demonstrating the application of such charge-labelled antibodies, we first tested the hypothesis in a simple experiment. In this experiments sEVs (derived from NSCLC cell line, H1975) were analysed using a sandwich type assay as described in chapter 5. First, the sEVs were captured on the sensor surface using biotinylated CD9 antibody as schematically shown in figure 6.2a. The surface was functionalized with a PPB-avidin protocol as described in chapter 4. With the intention to profile CD9 membrane proteins with detection probes, the captured sEVs were then conjugated with the same biotinylated-anti CD9 antibody as the detection probe. The signal obtained in these steps are presented as bar plots in figure 6.2b. At this point we wanted to verify the concept of charge labelling. As the

sEVs carry strong negative charge, a suitable electrostatic label for them should have positive charge in order to offer a strong charge contrast. We first chose to test avidin as a positively charged electrostatic label, whose binding to the detection antibody would generate a strong signal. There was indeed a fairly high signal from this binding, as shown in figure 6.2b. However, we also observed a large signal from the negative control which was recorded by injecting avidin without there being any detection antibodies bound to the sEVs. There non-specific interaction was likely between the avidin and the biotin terminals of the PPB layer underneath not covered by the sEVs, and possibly also with the lipid membrane of the sEVs due to electrostatic interactions. Nevertheless, the data clearly shows the prospect electrostatic labelling.

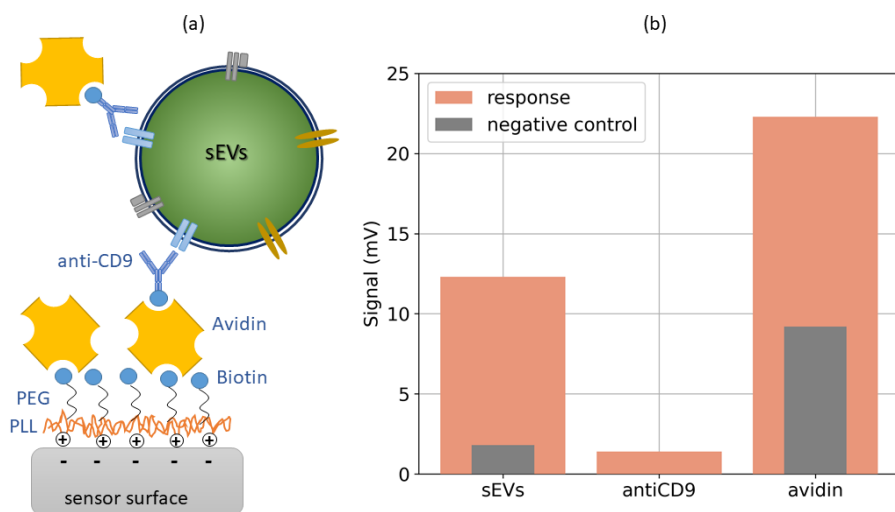


Figure 6.2. (a) A schematic representation of an sEV sandwich assay. The sEVs are first captured with a capture probe, and then their surface proteins are profiled with a detection probe (both were biotinylated antiCD9 in this case). (b) Bar plots of the signals obtained at various stages. The capture of the sEVs produces an expected large negative signal. At the next step, the signal generated by the detection probe was very weak. Then, avidin was used as a positively charged electrostatic label to enhance the signal. However, more than 40% of the signal generated by the avidin came from non-specific interactions.

Next, we tested PLL as a positively charged label. We chose it because its length can be controlled, allowing us to modulate the amount of charge it carries. While a longer length is desirable in order to increase its net charge, and hence the signal, it can also cause a larger NSB with the lipid membrane of the sEVs due to electrostatic interactions. Moreover, a longer PLL conjugated to an antibody can also potentially decrease its affinity to the corresponding surface protein. In chapter 5, we saw that increasing the length of the DNA conjugated to Z-domain seemed to reduce its affinity with the target. Hence,

for the present case, we decided to restrict the length of the PLL to 10 units. Note that the PLL used for labelling (hereafter referred to as PL10) was different from the PLL backbone of the PPB used in the surface functionalization, that had 100 units of L-lysine on average. For the labelling, the PLL was synthesized using solid state peptide synthesis (SPPS). They were then conjugated to Z-domain using Sortase A reaction, in a similar manner to the protocol described in the supplementary portion of Paper III [60]. Finally, this was used to label the antibodies using a photoconjugation reaction.

6.4 sEVs membrane protein profiling: biased vs. unbiased capture

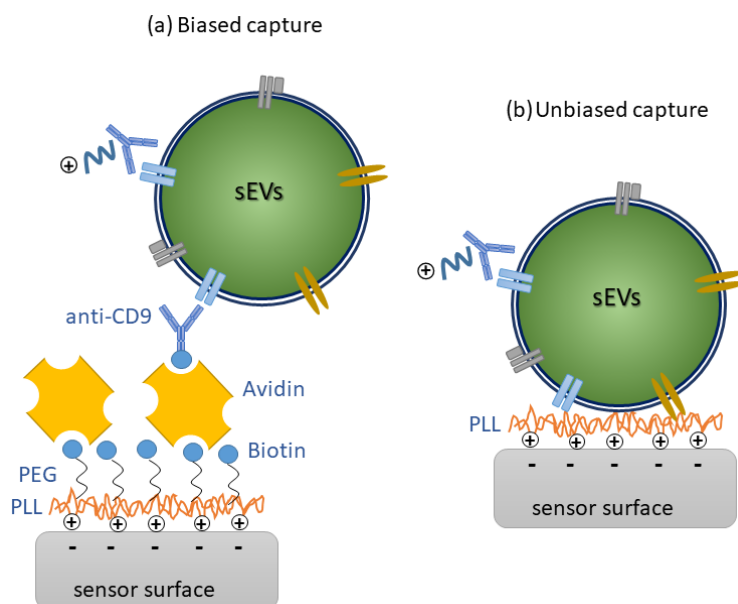


Figure 6.3. A schematic illustration indicating the two different approaches tested: (a) biased capture and (b) unbiased capture. In this case, anti-CD9 was used for the biased capture. The detection probe in both cases was anti-CD9 conjugated to PL10.

Having found a suitable candidate for a positively charged label, we proceeded to test its performance by conjugating it with the anti-CD9 antibody. We compared two different approaches for profiling the sEVs. Biased capture involved capturing the sEVs with a specific capture probe, such as anti-CD9, and then profiling the surface proteins of the captured population. Unbiased capture involved capturing the sEVs non-specifically on the PPB surface and then profiling their surface proteins. A schematic representation of both the

captures types is shown in figure 6.3. As evident, using the biased and unbiased strategies, we can interrogate different sEV subpopulations. We tested both the approaches (targeting the CD9-positive sEV population in case of the biased capture), and profiled the expression levels of CD9 and CD73 membrane proteins on the captured sEVs, in two separate experiments. The absolute values of the signals from the various steps are plotted in figure 6.4. We first observe that the signal from the direct assay step is much larger as compared to the sandwich assay step, which is similar to the simulations and the experimental results on sandwich assay discussed in chapter 5. We also note that signal is higher in case of the unbiased capture (18.8 ± 2.5) mV as compared to the biased capture (12.3 ± 2.1) mV. A possible reason is that the biased capture only results in the capture of the CD9 positive sEVs population, whereas the unbiased capture also includes those sEVs with small or no CD9 expression. Note that the signals are presented in absolute scale while the actual signal was negative as the baseline shifted lower (became more negative) due to the sEVs carrying negative charge. We then profiled both kinds of the captured sEVs for CD9 and CD73 expressions separately using the antiCD9 and antiCD73 detection probe respectively, both labelled with PL10.

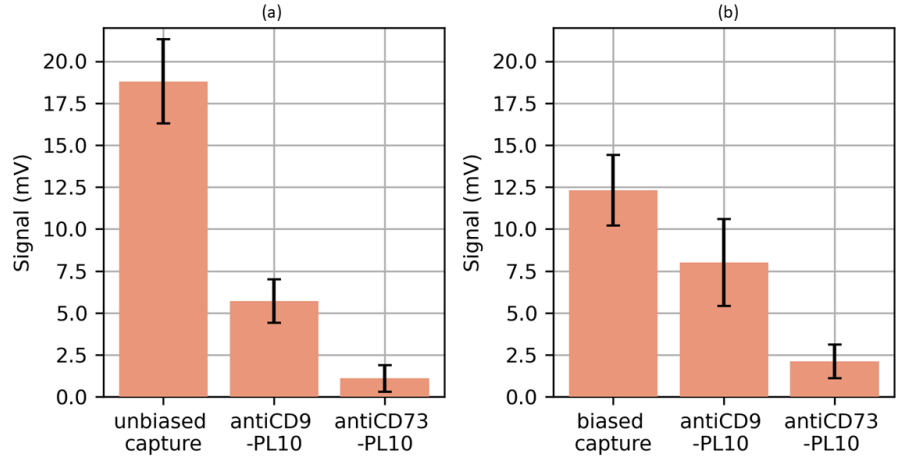


Figure 6.4. A comparison of the signals from (a) biased vs. (b) unbiased capture of sEVs and the subsequent profiling with antiCD9 and antiCD73 detection probe labelled with PL10. The two profiling steps were done in separate measurements. The signals indicate that less sEVs are captured in biased mode as compared to that in case of unbiased mode. Moreover, there is higher CD9 and CD73 expression on average in the captured sEVs population when the sEVs were specifically captured with antiCD9, as compared to the case of unbiased capture.

We observed that the signals from the profiling step of both CD9 and CD73 were higher in case of biased capture of sEVs as compared to the case of unbiased capture. This could be because of the fact that the average expression

levels of both were higher in case of the sEVs captured specifically with antiCD9 as compared to the unbiased capture. When comparing the signals in this way, we must note that the average values of ζ_i^* after the sEV capture, were different. In case of the unbiased capture it was -23.9 mV, while in case of the biased capture, it was -18.7 mV (data not shown). Despite a more negative baseline in case of the unbiased capture, which offered a higher charge contrast to the detection probes labelled with positive charges, we obtained a weaker signal from the profiling step with antiCD9. The comparison between the CD9 and CD73 levels is more straightforward, as both steps involved the same baseline after the corresponding sEV capturing step. In both cases, the CD9 level was clearly higher than the CD73 expression level. Moreover, both CD9 and CD73 expression levels were higher when the capture of sEVs was biased to the CD9 surface protein. This indicates a positive correlation between CD9 and CD73. The ability to identify such correlations among surface proteins is clinically relevant. For instance, the co-expression of CD39 and CD73 has been linked to the secretion of adenosine by the cells, that can act as an immuno-suppressor at later stages of cancer [92].

Table 6.1. The antibodies used along with the details of their conjugated electrostatic labels.

Antibody	Base	Label		
		Type	Length	Yield/Antibody
antiCD9-PL10	antiCD9	polylysine	10 units	1.3
antiCD73-PL10	antiCD73	polylysine	10 units	1.3
Cet-DNA15	cetuximab	DNA	15 nucleotides	1.1

6.5 Multi-marker profiling of extracellular vesicles

The sEVs sandwich assay opens up the possibility of detecting multiple surface markers on the captured sEVs. However, in order to carry out a step wise detection of several surface markers with electrostatic labels conjugated to the detection probes, we must choose alternating charge-labels. For instance, if we choose the first detection probe to be labelled with positive charge, then the second detection probe should have a negatively charged label in order to provide a sufficiently high charge contrast with the surface. This of course depends on the extent of the sEVs surface covered by the first detection probe so as to have a large enough impact on the overall surface charge. Here, we tested the expression of CD9 and EGFR surface proteins of the sEVs. For this, we used anti-CD9 conjugated to PL10, and cetuximab conjugated to DNA15. The sEVs were first subjected to unbiased capture on a PPB functionalized surface. Next, they were profiled with antiCD9-PL10. The same sEVs then underwent a second profiling step with Cet-DNA15. The schematic of the

multi-step method as well as the results are shown in figure 6.5. The bar plots indicate the magnitude of the signals obtained.

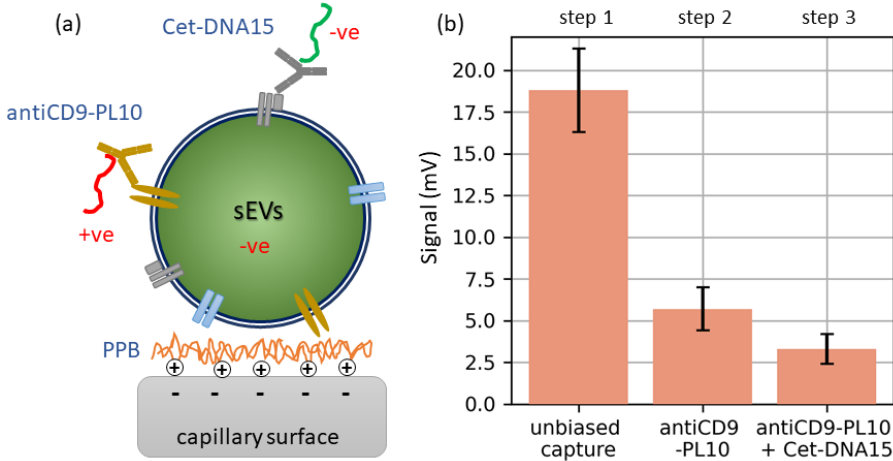


Figure 6.5. (a) Schematic showing the sequence of multi-step profiling of the CD9, followed by the EGFR expression levels, on the same population of sEVs captured non-specifically via PPB.

A key application of this multi-step profiling method is to analyse heterogeneity across different sEV populations. This could be different batches of sEVs, or sub-populations within the same batch isolated using biased capture. A limitation of the method is that the signal from each step is dependent on the signal from the preceding step due to the dependence of the sensor response of the preceding baseline. A direct comparison of the signals obtained from the sequential profiling steps on a captured sEV population should be done with a proper calibration plot that takes care of the influence of the baseline variation.

6.6 Chapter summary

In this chapter, we demonstrated a strategy to profile multiple membrane proteins of sEVs in order to analyse their heterogeneity. As the signal from the profiling step was rather weak, we used electrostatic labels to enhance it. Polylysine (10 units) and DNA (15 nucleotides) were identified as suitable charge labels for profiling the sEV surface proteins. Single-step profiling allowed us to probe and compare expression levels of CD9 and CD73 across biased and unbiased capture of sEVs. Biased capture leads to the capture of a larger number of sEVs as shown by the larger signal, but the expression level of CD9 and CD73 on average were higher in sEVs captured specifically with antiCD9 an-

tibodies. A strategy to carry out multi-step profiling of a captured sEV population was demonstrated using alternating charge-labels. This facilitates analysis of sEV heterogeneity by comparing the expression level of multiple surface proteins across different sEVs populations. It also opens up the possibility to carry out multiplexed detection of surface proteins using a single sensor channel.

7. Summary and Outlook

The work presented in this thesis has been an attempt to extend the scope of streaming current-based biosensing. It essentially boils down to understanding the interplay of charge distribution and ionic flow inside the electrical double layer and then exploiting the findings to achieve an improved sensitivity, specificity and novel applications. The main conclusions from the thesis are listed below.

Influence of the size and charge of the target:

- The signal of an electrokinetic biosensor depends on the size and charge of the proteins.
- This was demonstrated using a set of proteins that were captured covalently on the sensor surface.
- The sensitivity of the sensor varied over two orders of magnitude for the proteins studied.
- A pre-existing theoretical model was used to explain the results.
- The signal could be enhanced by changing the pH of the measurement buffer.

Surface charge manipulation for signal enhancement:

- An approach to enhance the signal of the sensor by tuning its surface charge was demonstrated.
- Three surface functionalization strategies were compared and the best signal was obtained for the one offering the maximum charge contrast between the sensor surface and the target.
- The improved technique was used to detect sEVs with an LOD that was two orders of magnitude enhanced compared to the previously reported method.
- This technique was further used for highly sensitive treatment monitoring of cancer cells as well as liquid biopsy with reduced sample volume, by profiling surface proteins of sEVs.

Electrokinetic sandwich assay:

- The proof of concept of an electrical immuno-sandwich assay was demonstrated.

- A better target selectivity and linear dependence on the concentration was demonstrated using trastuzumab as the target.
- The proof of concept was demonstrated both for a label-free version, as well as using DNA conjugation to enhance the signal.
- An application was demonstrated by detecting the target from a complex medium of PBS spiked with *E. coli* cell lysate.

Multi-marker profiling of sEVs with electrostatic labels:

- The concept of electrokinetic sandwich assay was applied to perform profiling of multiple membrane proteins of sEVs.
- Various potential labels were tested and PL10 and DNA15 were determined to be suitable ones.
- The profiling was done using a sequence of antibodies with alternating charge labels in order to take advantage of the influence of charge contrast on the signal
- This opens up the possibility to analyse the heterogeneity of sEVs across various sub-populations.

A lot of areas relating to these topics still remain unexplored, providing the basis for possible future investigation. In chapter 5, we demonstrated how the signal could be enhanced when DNA was conjugated with the detection probes. We however also observed a reduction in affinity between the target and the detection probe due to the presence of the DNA. This indicates the presence of an optimal length of the DNA that balances the signal enhancement and the affinity reduction. A study of the signal vs. length of the conjugated DNA could hence be useful in determining the optimal length. A similar investigation for the electrostatically labelled antibodies could also be useful for a better profiling of the sEVs.

We have discussed and compared three different surface functionalization strategies for modulating the surface charge for enhancing the signal in chapter 4. However, we did not manage to obtain a stable surface with a net positive charge in any of them. Despite introducing PLL and avidin on the silica surface, it still retained an overall negative ζ_i^* . We did observe the ζ_i^* being temporarily positive after PLL functionalization, but it slowly decayed and eventually attained equilibrium at a negative value (data not shown). We have not yet figured out a reason for this, as the electrostatic interaction between the PLL and silica is expected to be rather strong. This warrants further investigation. If we can obtain a positively charged silica surface either by tweaking the PLL functionalization, or choosing a different functionalization method altogether, we can enhance the sensitivity towards sEVs detection even further.

A major limitation we came across while analysing the signals in chapters 5 and 6 was that we cannot directly compare the bar plots to estimate whether

the capture of the target was higher as the values of ζ_i^* were different. This is because of the fact that the $\Delta\zeta^*$ depends on ζ_i^* . Further theoretical analysis is needed in order to be able to compare the signals obtained when the surface is functionalized with different capture probes. This would also be useful in comparing the expression level of different markers on the captured sEVs, even when the baseline after the binding of each detection probe is different.

Samfattning på svenska

Biosensorer baserade på jonströmmar är ett nytt och relativt utforskat område med stor potential. Denna avhandling ämnar fördjupa kunskaperna inom de underliggande principerna både för att ytterligare förbättra sensorernas prestation och även för att hitta nya tillämpningar. Teorin har studerats och två kritiska parametrar som påverkar sensorns känslighet har identifierats. Dessa var sensorns storlek och elektriska laddning. Parametrarna utvärderades experimentellt genom användandet av specialdesignade proteiner, med syfte att förstå parametrarnas natur och till vilken grad de påverkar sensorns respons. De teoretiska resultaten jämfördes sedan med simuleringar baserad på en etablerad modell.

Laddningen, eller mer specifikt, laddningskontrasten, mellan analyten och sensorns yta, påverkar sensorns respons. Genom att optimera funktionaliseringsstrategin av sensorytan öppnas ett nytt område upp när det gäller att förbättra sensorns känslighet och utveckla ny funktionalitet. Tre metoder jämfördes med avseende på den resulterande zetapotentialen på sensorns yta. Känsligheten var starkast när laddningskontrasten var som störst. Den optimala funktionaliseringsstrategin användes sedan för högkänslig detektion av extracellulära vesiklar, där en förbättring av detektionsgränsen på två storleksordningar i jämförelse med tidigare rapporterade resultat demonstrerades. Två tillämpningar av den förbättrade strategin förevisades sedan. Den första inom bevakning av effektiviteten av specifika mediciner för cancerbehandling. Den andra inom analys av vätskebiopsi på cancerpatienter genom känslig kartläggning av membranproteinen på extracellulära vesiklar.

Förbättring av detektionsspecificiteten är kritiskt inom biosensing. Detta skedde genom att implementera en sandwich-immunoanalys. Validering av konceptet gjordes genom att använda Z-domänen både som fångst- och som detektionssond för att detektera trastuzumab. Trots att selektiviteten förbättrades på bekostnaden av lägre känslighet kunde detta delvis motverkas genom att konjugera DNA med detektionssonden. Det här är en ny elektrostatisk kategoriseringsstrategi som möjliggör förbättrad känslighet genom att utnyttja detektionen från ett sammansatt medium av *E. Coli* cellysat. Följaktligen syntetiserades en grupp av positivt och negativt laddade antikroppar genom att länka polylysin respektive DNA-oligonukleotider. Detta möjliggjorde stegvis

multiplex analys av membranprotein på extracellulära vesiklar genom att använda antikroppar märkta med alternerande laddning. Denna metod användes sedan för att undersöka heterogeniteten hos extracellulära vesiklar.

Acknowledgements

A PhD is a marathon that is fraught with adventure along with uncertainties and roadblocks that can sometimes seem difficult to overcome. I was indebted to the guidance of my two very patient and supportive supervisors, Associate Prof. Apurba Dev and Prof. Shi-Li Zhang. I am grateful for their immense help in giving my PhD thesis the right direction, helpful discussions in designing the experiments, troubleshooting and interpreting the results. I am also glad for their constant feedback that polished my skills as a researcher and refine my critical thinking. I am heartily thankful to Prof. Jan Linnros for his feedback in several of the group meetings, and also his numerous visits to the lab, often in the late afternoons, to discuss my experiments and progress. His calming presence was often a great help during times of uncertainty.

I am grateful to my collaborators from the EP project, whose contributions were vital to my thesis. I am grateful to Prof. Amelie Eriksson Karlström for not only designing various kinds of probes as per our requirements, but also valuable discussions and feedback in my papers that improved my understanding of the biological side of my research project. I am also grateful to her group members: Christiane, Ábel and Maxime for their help. I am also very thankful to Dr. Kristina Viktorsson and Dr. Petra Hååg for providing us the EVs, valuable feedback on the results.

I owe a lot to my immediate colleagues Sara, Moein and Fredrik. Sara, I am very thankful for all your help, especially in the early days in the lab when I was struggling with the apparatus. It was also great to attend courses and work on assignments and group tasks together. Moein, thank you for all the help in the lab. It was always a pleasure to discuss new ideas and designs for your chip with you. Thanks also for all the car rides to and back from Stockholm, and for introducing me to Persian food. Thank you, Fredrik, for helping me with the fluorescence measurements, the Swedish translation of my thesis abstract, and the fun discussions, often over fika.

I am thankful to my colleagues Federico, Hithesh, Karthik, Jing, Adil and Lucy for their help at various points during my PhD. Several of my colleagues, such as Nishant, Sven, Faraz, Kostya also turned out to be great friends outside of the lab as well. Thanks Nishant for all the bike trips, random discussions, and the delicious meals. Thanks you, Sven for the numerous discussions about Sweden, politics, and sharing the princess cake when your father won it in the lottery.

I had a lot of fun teaching laboratory electronics alongside Uwe Zimmerman, Tomas Kubart, Tomas Nyberg, Chenyu and Corrado. I learnt a bit more about electronics along the way, while also troubleshooting the circuits and witnessing the occasional barbecue of the circuits that the students made.

I am grateful to the Sven Norén, Björn Kuzavas, and the rest of the MSL staff for their help in the cleanroom. Jonatan Bagge from the IT support and the staff at the mechanical workshop were quite helpful as well.

My time in Sweden would not have been as fun without some of the best friends that I made here. Thank you Sohan, Sumalata, Somendu, Shibu and Vlad for all the parties, board games, go-carting, cooking frenzies and biking trips. I made some lifelong memories with you all. I would also thank my housemate Ruben for all those cooking sessions, beer brewing, making pasta from scratch, wine and cheese tastings, and making me learn about various kinds of food from around the world.

Last, but certainly not the least, I would like to thank my parents and Shruti for their constant love and support. Thank you for sharing the joy from all my achievements so far, both big and small, and encouraging me on my tough days. You all are my strength and I would not have been able to come so far without you.

References

- [1] N. Bhalla, P. Jolly, N. Formisano, and P. Estrela, "Introduction to biosensors," *Essays Biochem.*, vol. 60, no. 1, p. 1, Jun. 2016.
- [2] W. S. Hughes, "THE POTENTIAL DIFFERENCE BETWEEN GLASS AND ELECTROLYTES IN CONTACT WITH THE GLASS," *J. Am. Chem. Soc.*, vol. 44, no. 12, pp. 2860–2867, Dec. 2002.
- [3] J. M. Nelson and E. G. Griffin, "ADSORPTION OF INVERTASE.," *J. Am. Chem. Soc.*, vol. 38, no. 5, pp. 1109–1115, May 2002.
- [4] E. G. Griffin and J. M. Nelson, "THE INFLUENCE OF CERTAIN SUBSTANCES ON THE ACTIVITY OF INVERTASE.," *J. Am. Chem. Soc.*, vol. 38, no. 3, pp. 722–730, Mar. 2002.
- [5] L. C. CLARK, R. WOLF, D. GRANGER, and Z. TAYLOR, "Continuous Recording of Blood Oxygen Tensions by Polarography," <https://doi.org/10.1152/jappl.1953.6.3.189>, vol. 6, no. 3, pp. 189–193, Sep. 1953.
- [6] M. J. Schöning and A. Poghossian, "Recent advances in biologically sensitive field-effect transistors (BioFETs)," *Analyst*, vol. 127, no. 9, pp. 1137–1151, Sep. 2002.
- [7] P. Bergveld, "Development of an ion-sensitive solid-state device for neurophysiological measurements," *IEEE Trans. Biomed. Eng.*, vol. 17, no. 1, pp. 70–71, 1970.
- [8] E. H. Yoo and S. Y. Lee, "Glucose biosensors: an overview of use in clinical practice," *Sensors (Basel)*, vol. 10, no. 5, pp. 4558–4576, May 2010.
- [9] B. Liedberg, C. Nylander, and I. Lunström, "Surface plasmon resonance for gas detection and biosensing," *Sensors and Actuators*, vol. 4, no. C, pp. 299–304, Jan. 1983.
- [10] M. C. Vestergaard, K. Kerman, I. M. Hsing, and E. Tamiya, "Nanobiosensors and nanobioanalyses," *Nanobiosensors and Nanobioanalyses*, pp. 1–379, Jan. 2015.
- [11] N. Akkilic, S. Geschwindner, and F. Höök, "Single-molecule biosensors: Recent advances and applications," *Biosens. Bioelectron.*, vol. 151, p. 111944, Mar. 2020.
- [12] P.-C. Chen *et al.*, "Editors' Choice—Field-Effect Transistor-Based Biosensors and a Portable Device for Personal Healthcare," *ECS J. Solid State Sci. Technol.*, vol. 6, no. 7, p. Q71, Jun. 2017.
- [13] T. Terse-Thakoor, S. Badhulika, and A. Mulchandani, "Graphene based biosensors for healthcare," *J. Mater. Res.*, vol. 32, no. 15, pp. 2905–2929, Aug. 2017.
- [14] J. Kim, A. S. Campbell, B. E. F. de Ávila, and J. Wang, "Wearable biosensors for healthcare monitoring," *Nat. Biotechnol.* 2019 374, vol. 37, no. 4, pp. 389–406, Feb. 2019.

- [15] S. Hassani *et al.*, “Biosensors and their applications in detection of organophosphorus pesticides in the environment,” *Arch. Toxicol.* 2016 911, vol. 91, no. 1, pp. 109–130, Oct. 2016.
- [16] M. Badihi-Mossberg, V. Buchner, and J. Rishpon, “Electrochemical Biosensors for Pollutants in the Environment,” *Electroanalysis*, vol. 19, no. 19–20, pp. 2015–2028, Oct. 2007.
- [17] E. C. Alocilja and S. M. Radke, “Market analysis of biosensors for food safety,” *Biosens. Bioelectron.*, vol. 18, no. 5–6, pp. 841–846, May 2003.
- [18] A. Amine, H. Mohammadi, I. Bourais, and G. Palleschi, “Enzyme inhibition-based biosensors for food safety and environmental monitoring,” *Biosens. Bioelectron.*, vol. 21, no. 8, pp. 1405–1423, Feb. 2006.
- [19] R. Baronas, J. Kulys, A. Lančinskas, and A. Žilinskas, “Effect of Diffusion Limitations on Multianalyte Determination from Biased Biosensor Response,” *Sensors (Basel)*, vol. 14, no. 3, p. 4634, Mar. 2014.
- [20] J. Garcia-Guirado *et al.*, “Overcoming Diffusion-Limited Biosensing by Electrothermoplasmonics,” *ACS Photonics*, vol. 5, no. 9, pp. 3673–3679, Sep. 2018.
- [21] D. Juncker, S. Bergeron, V. Laforte, and H. Li, “Cross-reactivity in antibody microarrays and multiplexed sandwich assays: shedding light on the dark side of multiplexing,” *Curr. Opin. Chem. Biol.*, vol. 18, no. 1, pp. 29–37, Feb. 2014.
- [22] D. Liu *et al.*, “Trends in miniaturized biosensors for point-of-care testing,” *TrAC Trends Anal. Chem.*, vol. 122, p. 115701, Jan. 2020.
- [23] L. J. Wang, Y. C. Chang, R. Sun, and L. Li, “A multichannel smartphone optical biosensor for high-throughput point-of-care diagnostics,” *Biosens. Bioelectron.*, vol. 87, pp. 686–692, Jan. 2017.
- [24] Y. Tepeli and A. Ülkü, “Electrochemical biosensors for influenza virus a detection: The potential of adaptation of these devices to POC systems,” *Sensors Actuators B Chem.*, vol. 254, pp. 377–384, Jan. 2018.
- [25] H. Shafiee *et al.*, “Paper and Flexible Substrates as Materials for Biosensing Platforms to Detect Multiple Biotargets,” *Sci. Reports 2015 51*, vol. 5, no. 1, pp. 1–9, Mar. 2015.
- [26] E. Ghafar-Zadeh, “Wireless Integrated Biosensors for Point-of-Care Diagnostic Applications,” *Sensors 2015, Vol. 15, Pages 3236-3261*, vol. 15, no. 2, pp. 3236–3261, Feb. 2015.
- [27] J. R. Choi, “Development of Point-of-Care Biosensors for COVID-19,” *Front. Chem.*, vol. 8, p. 517, May 2020.
- [28] Grand View Research, “Biosensors Market Size | Global Industry Report, 2021-2028,” 2021.
- [29] C. R. Paul, *Fundamentals of electric circuit analysis*. John Wiley & Sons, 2001.
- [30] D. C. Martins, V. Chu, D. M. F. Prazeres, and J. P. Conde, “Streaming currents in microfluidics with integrated polarizable electrodes,” *Microfluid. Nanofluidics*, vol. 15, no. 3, pp. 361–376, Sep. 2013.
- [31] P. Leroy, N. Devau, A. Revil, and M. Bizi, “Influence of surface conductivity on the apparent zeta potential of amorphous silica nanoparticles,” *J. Colloid Interface Sci.*, vol. 410, pp. 81–93, Nov. 2013.
- [32] D. E. Yates, S. Levine, and T. W. Healy, “Site-binding model of the electrical double layer at the oxide/water interface,” *J. Chem. Soc. Faraday Trans. 1 Phys. Chem. Condens. Phases*, vol. 70, no. 0, pp. 1807–1818, Jan. 1974.
- [33] B. J. Kirby, *Micro- and Nanoscale Fluid Mechanics: Transport in Microfluidic Devices*. Cambridge University Press, 2010.

- [34] Z. Adamczyk, K. Sadlej, E. Wajnryb, M. Nattich, M. L. Ekiel-Jezewska, and J. Bławdziewicz, "Streaming potential studies of colloid, polyelectrolyte and protein deposition," *Adv. Colloid Interface Sci.*, vol. 153, no. 1–2, pp. 1–29, 2010.
- [35] R. A. Hayes, "The electrokinetic behaviour of surfaces modified by particle adsorption," *Colloids Surfaces A Physicochem. Eng. Asp.*, vol. 146, no. 1–3, pp. 89–94, 1999.
- [36] A. P. Michelmore and R. A. Hayes, "The effect of deposition of negatively charged particles on the electrokinetic behaviour of oppositely charged surfaces," *PhysChemComm*, vol. 3, no. 1, 2000.
- [37] R. A. Hayes, M. R. Böhmmer, and L. G. J. Fokkink, "Study of silica nanoparticle adsorption using optical reflectometry and streaming potential techniques," *Langmuir*, vol. 15, no. 8, pp. 2865–2870, 1999.
- [38] K. Sadlej, E. Wajnryb, J. Bawdziewicz, M. L. Ekiel-Jeewska, and Z. Adamczyk, "Streaming current and streaming potential for particle covered surfaces: Virial expansion and simulations," *J. Chem. Phys.*, vol. 130, no. 14, 2009.
- [39] M. Zembala, Z. Adamczyk, and P. Warszyński, "Streaming potential of mica covered by latex particles," *Colloids Surfaces A Physicochem. Eng. Asp.*, vol. 222, no. 1–3, pp. 329–339, 2003.
- [40] M. L. Ekiel-Jezewska, Z. Adamczyk, and J. Bławdziewicz, "Streaming Current and Effective ζ -Potential for Particle-Covered Surfaces with Random Particle Distributions," *J. Phys. Chem. C*, vol. 123, no. 6, pp. 3517–3531, Feb. 2019.
- [41] H. P. Erickson, "Size and shape of protein molecules at the nanometer level determined by sedimentation, gel filtration, and electron microscopy," *Biol. Proced. Online*, vol. 11, no. 1, pp. 32–51, 2009.
- [42] M. Kaszuba, J. Corbett, F. M. N. Watson, and A. Jones, "High-concentration zeta potential measurements using light-scattering techniques," *Philos. Trans. R. Soc. A Math. Phys. Eng. Sci.*, vol. 368, no. 1927, pp. 4439–4451, Sep. 2010.
- [43] G. Midekessa *et al.*, "Zeta Potential of Extracellular Vesicles: Toward Understanding the Attributes that Determine Colloidal Stability," *ACS Omega*, vol. 5, no. 27, pp. 16701–16710, Jul. 2020.
- [44] S. Cavallaro *et al.*, "Multiparametric Profiling of Single Nanoscale Extracellular Vesicles by Combined Atomic Force and Fluorescence Microscopy: Correlation and Heterogeneity in Their Molecular and Biophysical Features," *Small*, vol. 17, no. 14, p. 2008155, Apr. 2021.
- [45] I. Stevic, G. Buescher, and F. L. Ricklefs, "Monitoring Therapy Efficiency in Cancer through Extracellular Vesicles," *Cells*, vol. 9, no. 1. NLM (Medline), p. 130, 06-Jan-2020.
- [46] E. Oeyen *et al.*, "Determination of variability due to biological and technical variation in urinary extracellular vesicles as a crucial step in biomarker discovery studies," *J. Extracell. Vesicles*, vol. 8, no. 1, Dec. 2019.
- [47] M. Santarpia *et al.*, "Liquid biopsy for lung cancer early detection," *Journal of Thoracic Disease*, vol. 10, no. Suppl 7. AME Publishing Company, pp. S882–S897, 01-Apr-2018.
- [48] C. Stiller *et al.*, "Detection of tumor-associated membrane receptors on extracellular vesicles from non-small cell lung cancer patients via immunopcr," *Cancers (Basel)*, vol. 13, no. 4, pp. 1–21, Feb. 2021.
- [49] J. Vykoukal *et al.*, "Plasma-derived extracellular vesicle proteins as a source of biomarkers for lung adenocarcinoma," *Oncotarget*, vol. 8, no. 56, pp. 95466–95480, Sep. 2017.

- [50] K. Liang *et al.*, “Nanoplasmonic quantification of tumour-derived extracellular vesicles in plasma microsamples for diagnosis and treatment monitoring,” *Nat. Biomed. Eng.*, vol. 1, no. 4, p. 21, Apr. 2017.
- [51] S. Cavallaro *et al.*, “Label-free surface protein profiling of extracellular vesicles by an electrokinetic sensor,” *ACS Sensors*, vol. 4, no. 5, pp. 1399–1408, Apr. 2019.
- [52] A. Dev *et al.*, “Electrokinetic effect for molecular recognition: A label-free approach for real-time biosensing,” *Biosens. Bioelectron.*, vol. 82, pp. 55–63, 2016.
- [53] S. S. Sahu, C. Stiller, S. Cavallaro, A. E. Karlström, J. Linnros, and A. Dev, “Influence of molecular size and zeta potential in electrokinetic biosensing,” *Biosens. Bioelectron.*, vol. 152, no. December 2019, 2020.
- [54] M. Zembala and Z. Adamczyk, “Measurements of streaming potential for mica covered by colloid particles,” *Langmuir*, vol. 16, no. 4, pp. 1593–1601, 2000.
- [55] J. Löfblom, J. Feldwisch, V. Tolmachev, J. Carlsson, S. Ståhl, and F. Y. Frejd, “Affibody molecules: Engineered proteins for therapeutic, diagnostic and biotechnological applications,” *FEBS Lett.*, vol. 584, no. 12, pp. 2670–2680, Jun. 2010.
- [56] J. Horak *et al.*, “Recombinant Spider Silk as Mediator for One-Step, Chemical-Free Surface Biofunctionalization,” *Adv. Funct. Mater.*, vol. 28, no. 21, May 2018.
- [57] A. Lošdorfer Božič and R. Podgornik, “pH Dependence of Charge Multipole Moments in Proteins,” *Biophys. J.*, vol. 113, no. 7, pp. 1454–1465, Oct. 2017.
- [58] S. Das, S. Chakraborty, and S. K. Mitra, “Redefining electrical double layer thickness in narrow confinements: Effect of solvent polarization,” *Phys. Rev. E - Stat. Nonlinear, Soft Matter Phys.*, vol. 85, no. 5, May 2012.
- [59] A. Garai and S. Chakraborty, “Steric effect and slip-modulated energy transfer in narrow fluidic channels with finite aspect ratios,” *Electrophoresis*, vol. 31, no. 5, pp. 843–849, Mar. 2010.
- [60] S. S. Sahu *et al.*, “Electrokinetic sandwich assay and DNA mediated charge amplification for enhanced sensitivity and specificity,” *Biosens. Bioelectron.*, vol. 176, p. 112917, Mar. 2021.
- [61] M. J. O’Brien II, S. R. J. Brueck, V. H. Perez-Luna, L. M. Tender, and G. P. Lopez, “SPR biosensors: simultaneously removing thermal and bulk-composition effects| This paper was presented at the Fifth World Congress on Biosensors, Berlin, Germany, 3–5 June 1998.1,” *Biosens. Bioelectron.*, vol. 14, no. 2, pp. 145–154, Feb. 1999.
- [62] M. M. Rahman, M. M. Rana, M. S. Rahman, M. S. Anower, M. A. Mollah, and A. K. Paul, “Sensitivity enhancement of SPR biosensors employing heterostructure of PtSe2 and 2D materials,” *Opt. Mater. (Amst.)*, vol. 107, p. 110123, Sep. 2020.
- [63] A. van den Berg, P. Bergveld, D. N. Reinhoudt, and E. J. Sudhölter, “Sensitivity control of ISFETs by chemical surface modification,” *Sensors and Actuators*, vol. 8, no. 2, pp. 129–148, Oct. 1985.
- [64] A. Rivadeneyra, J. Fernández-Salmerón, J. Banqueri, J. A. López-Villanueva, L. F. Capitan-Vallvey, and A. J. Palma, “A novel electrode structure compared with interdigitated electrodes as capacitive sensor,” *Sensors Actuators B Chem.*, vol. 204, pp. 552–560, Dec. 2014.
- [65] Y. L. Yang, L. H. Lo, I. Y. Huang, H. J. H. Chen, W. S. Huang, and S. R. S. Huang, “Improvement of Polyimide Capacitive Humidity Sensor by Reactive Ion Etching and Novel Electrode Design,” *Proc. IEEE Sensors*, vol. 1, no. 1, pp. 511–514, 2002.

- [66] N. S. K. Gunda, M. Singh, L. Norman, K. Kaur, and S. K. Mitra, "Optimization and characterization of biomolecule immobilization on silicon substrates using (3-aminopropyl)triethoxysilane (APTES) and glutaraldehyde linker," *Appl. Surf. Sci.*, vol. 305, pp. 522–530, Jun. 2014.
- [67] L. Liu, K. C. Etika, K. S. Liao, L. A. Hess, D. E. Bergbreiter, and J. C. Grunlan, "Comparison of covalently and noncovalently functionalized carbon nanotubes in epoxy," *Macromol. Rapid Commun.*, vol. 30, no. 8, pp. 627–632, Apr. 2009.
- [68] Y. Zhang, C.-W. Chu, W. Ma, and A. Takahara, "Functionalization of Metal Surface via Thiol–Ene Click Chemistry: Synthesis, Adsorption Behavior, and Postfunctionalization of a Catechol- and Allyl-Containing Copolymer," *ACS Omega*, 2020.
- [69] S. Cavallaro *et al.*, "Multiplexed electrokinetic sensor for detection and therapy monitoring of extracellular vesicles from liquid biopsies of non-small-cell lung cancer patients," *Biosens. Bioelectron.*, vol. 193, Apr. 2021.
- [70] S. S. Sahu *et al.*, "Exploiting Electrostatic Interaction for Highly Sensitive Detection of Tumor-Derived Extracellular Vesicles by an Electrokinetic Sensor," *ACS Appl. Mater. Interfaces*, vol. 13, pp. 42513–42521, 2021.
- [71] M. Morga, Z. Adamczyk, S. Gödrich, M. Oćwieja, and G. Papastavrou, "Monolayers of poly-L-lysine on mica - Electrokinetic characteristics," *J. Colloid Interface Sci.*, vol. 456, pp. 116–124, Oct. 2015.
- [72] M. Lepoitevin, B. Jamilloux, M. Bechelany, E. Balanzat, J. M. Janot, and S. Balme, "Fast and reversible functionalization of a single nanopore based on layer-by-layer polyelectrolyte self-assembly for tuning current rectification and designing sensors," *RSC Adv.*, vol. 6, no. 38, pp. 32228–32233, Mar. 2016.
- [73] P. T. Charles, V. R. Stubbs, C. M. Soto, B. D. Martin, B. J. White, and C. R. Taitt, "Reduction of non-specific protein adsorption using poly(ethylene) glycol (PEG) modified polyacrylate hydrogels in immunoassays for staphylococcal enterotoxin B detection," *Sensors*, vol. 9, no. 1, pp. 645–655, Jan. 2009.
- [74] D. König, S. S. Prince, and S. I. Rothschild, "Targeted therapy in advanced and metastatic non-small cell lung cancer. An update on treatment of the most important actionable oncogenic driver alterations," *Cancers*, vol. 13, no. 4. MDPI AG, pp. 1–37, 02-Feb-2021.
- [75] N. Abdel Karim and K. Kelly, "Role of Targeted Therapy and Immune Checkpoint Blockers in Advanced Non-Small Cell Lung Cancer: A Review," *Oncologist*, vol. 24, no. 9, pp. 1270–1284, Sep. 2019.
- [76] M. Kang *et al.*, "Programmed death-ligand 1 expression level as a predictor of EGFR tyrosine kinase inhibitor efficacy in lung adenocarcinoma," *Transl. Lung Cancer Res.*, vol. 10, no. 2, pp. 699–711, Feb. 2021.
- [77] D. H. Kim *et al.*, "Exosomal PD-L1 promotes tumor growth through immune escape in non-small cell lung cancer," *Exp. Mol. Med.*, vol. 51, no. 8, pp. 1–13, Aug. 2019.
- [78] N. Zhang *et al.*, "The EGFR pathway is involved in the regulation of PD-L1 expression via the IL-6/JAK/STAT3 signaling pathway in EGFR-mutated non-small cell lung cancer," *Int. J. Oncol.*, vol. 49, no. 4, pp. 1360–1368, Oct. 2016.
- [79] Z. Ge and Y. Wang, "Estimation of Nanodiamond Surface Charge Density from Zeta Potential and Molecular Dynamics Simulations," *J. Phys. Chem. B*, vol. 121, no. 15, pp. 3394–3402, Apr. 2017.
- [80] J. Y. Lichtenberg, Y. Ling, and S. Kim, "Non-specific adsorption reduction methods in biosensing," *Sensors (Switzerland)*, vol. 19, no. 11. MDPI AG, 01-Jun-2019.

- [81] X. Pei, B. Zhang, J. Tang, B. Liu, W. Lai, and D. Tang, "Sandwich-type immunosensors and immunoassays exploiting nanostructure labels: A review," *Anal. Chim. Acta*, vol. 758, pp. 1–18, Jan. 2013.
- [82] S. Kim and H. J. Lee, "Gold Nanostar Enhanced Surface Plasmon Resonance Detection of an Antibiotic at Attomolar Concentrations via an Aptamer-Antibody Sandwich Assay," *Anal. Chem.*, vol. 89, no. 12, pp. 6624–6630, 2017.
- [83] B. Shui, D. Tao, J. Cheng, Y. Mei, N. Jaffrezic-Renault, and Z. Guo, "A novel electrochemical aptamer-antibody sandwich assay for the detection of tau-381 in human serum," *Analyst*, vol. 143, no. 15, pp. 3549–3554, 2018.
- [84] D. Sun, J. Lu, L. Zhang, and Z. Chen, "Aptamer-based electrochemical cytosensors for tumor cell detection in cancer diagnosis: A review," *Anal. Chim. Acta*, vol. 1082, pp. 1–17, 2019.
- [85] D. Tang and J. Ren, "In Situ Amplified Electrochemical Immunoassay for Carcinoembryonic Antigen Using Horseradish Peroxidase-Encapsulated Nanogold Hollow Microspheres as Labels," *Anal. Chem.*, vol. 80, no. 21, pp. 8064–8070, Nov. 2008.
- [86] B. Su, J. Tang, H. Chen, J. Huang, G. Chen, and D. Tang, "Thionine/nanogold multilayer film for electrochemical immunoassay of alpha-fetoprotein in human serum using biofunctional double-codified gold nanoparticles," *Anal. Methods*, vol. 2, no. 11, pp. 1702–1709, Nov. 2010.
- [87] R. Cui, H. C. Pan, J. J. Zhu, and H. Y. Chen, "Versatile immunosensor using CdTe quantum dots as electrochemical and fluorescent labels," *Anal. Chem.*, vol. 79, no. 22, pp. 8494–8501, Nov. 2007.
- [88] M. Ultsch, A. Braisted, H. R. Maun, and C. Eigenbrot, "3-2-1: Structural insights from stepwise shrinkage of a three-helix Fc-binding domain to a single helix," *Protein Eng. Des. Sel.*, vol. 30, no. 9, pp. 619–625, Sep. 2017.
- [89] Y. Ishihama *et al.*, "Protein abundance profiling of the Escherichia coli cytosol," *BMC Genomics*, vol. 9, pp. 1–17, 2008.
- [90] R. T. K. Kwok, C. W. T. Leung, J. W. Y. Lam, and B. Z. Tang, "Biosensing by luminogens with aggregation-induced emission characteristics," *Chem. Soc. Rev.*, vol. 44, no. 13, pp. 4228–4238, Jun. 2015.
- [91] A. Gevari, M. T., Sahu, S. S., Mitra, D., Linnros, J., Dev, "Microchip-based electrokinetic biosensor: microfabrication and application in membrane protein profiling of exosomes."
- [92] V. Vautrot, H. Bentayeb, S. Causse, C. Garrido, and J. Gobbo, "Tumor-Derived Exosomes: Hidden Players in PD-1/PD-L1 Resistance," *Cancers* 2021, Vol. 13, Page 4537, vol. 13, no. 18, p. 4537, Sep. 2021.

Acta Universitatis Upsaliensis

*Digital Comprehensive Summaries of Uppsala Dissertations
from the Faculty of Science and Technology 2120*

Editor: The Dean of the Faculty of Science and Technology

A doctoral dissertation from the Faculty of Science and Technology, Uppsala University, is usually a summary of a number of papers. A few copies of the complete dissertation are kept at major Swedish research libraries, while the summary alone is distributed internationally through the series Digital Comprehensive Summaries of Uppsala Dissertations from the Faculty of Science and Technology. (Prior to January, 2005, the series was published under the title "Comprehensive Summaries of Uppsala Dissertations from the Faculty of Science and Technology".)



ACTA
UNIVERSITATIS
UPSALIENSIS
UPPSALA
2022

Distribution: publications.uu.se
urn:nbn:se:uu:diva-467813